LA UNIVERSIDAD EN INTERNET

UNIVERSITAT ROVIRA i VIRGILI

Escuela Superior de Ingeniería y Tecnología

Escola Tècnica Superior d'Enginyeria Química

Master's Thesis

Master's Degree in Computational Fluid Dynamics

Modelling the flow inside closed aquaculture rearing systems

Presented by: López Biagi, José Ricardo

Director: Martorell Masip, Benjamí

Date: 22/09/2020

Este trabajo está dedicado a la memoria
de Ana María de Buen López de Heredia
y de su padre, Sadí de Buen Lozano.

Recorriendo este camino, el sonido de
mis pasos le hace eco a los senderos
que trazaron en nuestros recuerdos.

Acknowledgements

I would like to thank Ingve Karlsen, Tore Birkeland and John Knudsen for the trust and the support which made this year of studies possible.

I would also like to thank my thesis director, Dr. Benjamí Martorell Masip, for his advice and guidance throughout the development of this work.

Table of Contents

List of figures

List of tables

Notation

BL - body lengths
CFD - Computational Fluid Dynamics
DO - Dissolved Oxygen
HRT - Hydraulic Retention Time
RAS - Recirculating Aquaculture System
Re - Reynolds number
RSM - Reynolds Stress Model
SIMPLE - Semi-Implicit Method for Pressure Linked Equations
TAN - total ammonia nitrogen
TDV - Total Variation Diminishing
VOF - Volume Of Fluid
k - turbulent kinetic energy
β - angular momentum
β_0 - angular momentum in the tank center
β_w - angular momentum at the tank wall
ε - turbulent dissipation rate

ν - kinematic viscosity

ν_T - eddy viscosity

ρ - water density

τ_0 - average boundary shear stress

τ_w - wall shear stress

Ω - angular velocity

ω - specific dissipation rate

C_t - tank resistance coefficient

F_i - impulse force

A - surface area

C_d - friction coefficient

D - tank diameter

d_h - hydraulic diameter

H - water column height

I - turbulence intensity

l - turbulent length scale

P_i - power input

Q - volumetric flow rate

Q_c - thershold volumetric flow rate

R - outer tank radius

r - radial distance from the axis

$T_{r,f}$ - resistance torque at the floor

$T_{r,s}$ - resistance torque generated by a structure

$T_{r,w}$ - resistance torque at the walls

T_i - input torque

T_r - resistance torque

V - tank volume

V_1 - circulating veloctiy in the tank

V_{in} - inlet jet velocity

V_r - radial velocity

V_θ - tangential velocity

y^+ - dimensionless wall distance

Resumen

La piscicultura es una industria en crecimiento, así como las dimensiones de los tanques de cultivo, donde velocidades de nado adecuadas son un requisito fundamental. La hidrodinámica en tanques con diámetros de hasta 10 m ha sido documentada, pero se conoce poco sobre la hidrodinámica en estructuras más grandes. El objetivo principal de este trabajo ha sido la implementación y validación de un modelo CFD (OpenFOAM) para representar el flujo en tanques pequeños con 1.5 m de diámetro. Posteriormente, la metodología validada ha sido aplicada a tanques con diámetros de 5 a 40 m. Las características principales del flujo – un vórtice forzado y un vórtice de "bañera" – han sido correctamente modeladas con la implementación del modelo de turbulencia RANS $k-\varepsilon$ realizable en tanques con diámetros de hasta 10 m. Los resultados indican que en estructuras más grandes el vórtice de "bañera" se disipa como consecuencia de mayores niveles de turbulencia.

Palabras Clave: CFD, OpenFOAM, vórtice de la bañera, hidrodinámica en tanques, piscicultura.

Abstract

Aquaculture is a growing industry and so are the sizes of closed rearing units, where adequate fish swimming speeds are paramount. The hydrodynamics in closed tanks of up to 10 m in diameter have been documented, but there is little information on larger structures. The main purpose of this work has been the implementation and validation of a CFD (OpenFOAM) model to represent the hydrodynamics inside circular aquaculture tanks with a diameter of 1.5 m. Subsequently, the validated modelling procedure was applied to tanks with diameters ranging from 5 to 40 m. It was found that when using the realizable $k-\varepsilon$ RANS turbulence model, the most important flow characteristics – a forced and a bathtub vortex – are successfully modelled in tanks with a diameter of up to 10 m. Results suggest that in larger structures, higher turbulence levels result in the dissipation of the bathtub vortex.

Keywords: Computational Fluid Dynamics (CFD), OpenFOAM, bathtub vortex, tank hydrodynamics, aquaculture

1. Introduction

With the growing world population, there is a rising demand of protein resources worldwide, fish being one of them. Nevertheless, capture fisheries have reached their annual production plateau at around 90 million tonnes due to the overexploitation of natural resources, making aquaculture an ever more relevant alternative.

From 1980 to 2018, the global annual aquaculture production has increased more than twentyfold, reaching 82.1 tonnes in 2018, with fin fish accounting for roughly 60% of the total production. By 2030 annual aquaculture production is projected to reach 109 tonnes (*The State of World Fisheries and Aquaculture 2020*, 2020).

There is an ever-increasing pressure on the utilization of aquaculture resources (land, coastal areas, water and feed resources, to name some), which has resulted in the improvement of existing techniques and the development of new ones. This has also led to more research in numerous fields, spanning from fish health, growth and behaviour (Dalsgaard et al., 2013; Thorarensen & Farrell, 2011) to the development of production facilities and processes (Chu et al., 2020; Terjesen et al., 2013). Although the number of published papers increases from year to year, the fields of study are extremely vast. For instance, each fish species has very different and complex growing conditions, which must be first understood to design efficient production facilities.

Figure 1. Examples of open net cages.

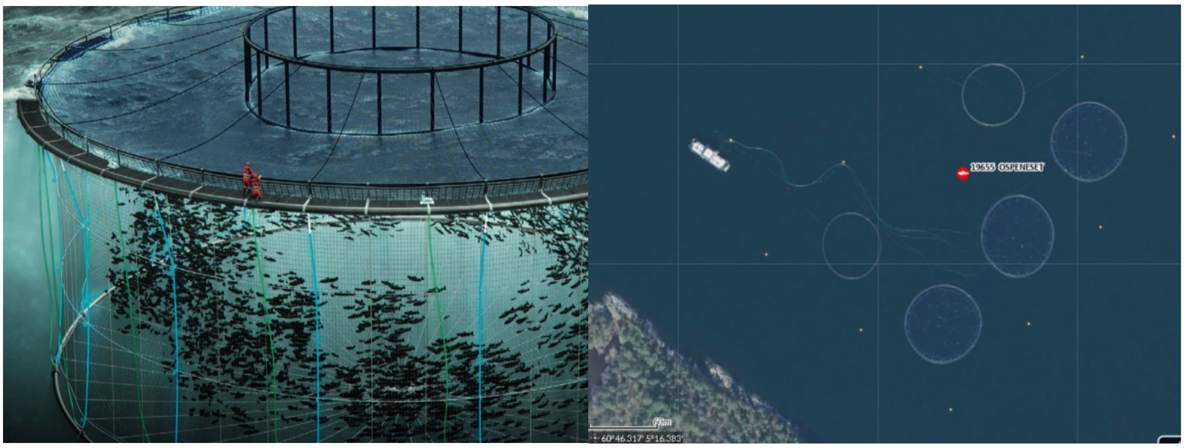

Note. Single open net cage (left) and production plant with feeder barge (right).
Sources. (Scale AQ, 2020)(left), (Fiskeridirektoratet, 2020) (right)

Norway, which is the second biggest exporter of fish products after China, has the largest aquaculture sector for salmonids in the world (*The State of World Fisheries and Aquaculture 2020*, 2020), and is an interesting reference case, as it is a global leader in innovation in the sector. Traditionally, salmonid production in Norway has been carried out in seawater open net cage systems (Figure 1) as the Norwegian fjords offer relatively well sheltered areas. In 2018, there was a total of 1015 production sites in seawater (mostly open net cage systems) and only 215 production sites in land (most of which are dedicated to smolt production) with a total production of 1,349,758 tons (*Key Figures from Norwegian Aquaculture Industry 2018*, 2019).

Open cage systems have a negative impact on the environment due to water pollution via fish waste, uneaten feed and chemical treatments, and pose a threat to native fish species in the event of fish escape and through the spread of parasites and diseases (Colbourne, 2005; Huguenin, 1997; Nordi et al., 2011; Shainee et al., 2013; Taranger et al., 2015; Verhoeven et al., 2018). In order to address these issues and to cope with the limitations associated with the opening of new near-shore sites, three possible solutions are off-shore structures, land based sites and floating closed containment systems (CCS).

Closed rearing systems offer a series of advantages in concurrence with many challenges. They offer an isolated environment in which water quality, velocities, and temperatures can be controlled. The risk of fish escape is eliminated or greatly reduced, as is the risk of infection from external pathogens. Sea lice, for instance, can be a big problem in open net cage installations, and mechanical separation is a very sound practice as it does not involve the use of any harmful substances and it does not contribute to the evolution of treatment-resistance sea lice (Nilsen et al., 2017). These advantages result in higher fish stocking densities when compared to traditional open systems.

The above mentioned points come at a price, as investment capitals and operational costs – related to power consumption, water treatment and monitoring systems – are higher (Chu et al., 2020). According to Gorle et al. (2018), CCS plants could account for 500,000 tons of production in Norway by 2030, which equals 37% of the total salmonid production of 2018.

In the last years, several solutions and concepts have been developed. Some examples are the Ecocage (Figure 2), the FishGlobe and the Egget (Figure 3). CCS technology is still under development, and no universal or standard solution exists. The response of these structures to environmental forces is very different to the highly dampened response of open net cages (Lader et al., 2017; Strand et al., 2013), and the rearing environment, as already mentioned, needs continuous monitoring and controlling.

Figure 2. The Ecomerd, a semi-closed CCS

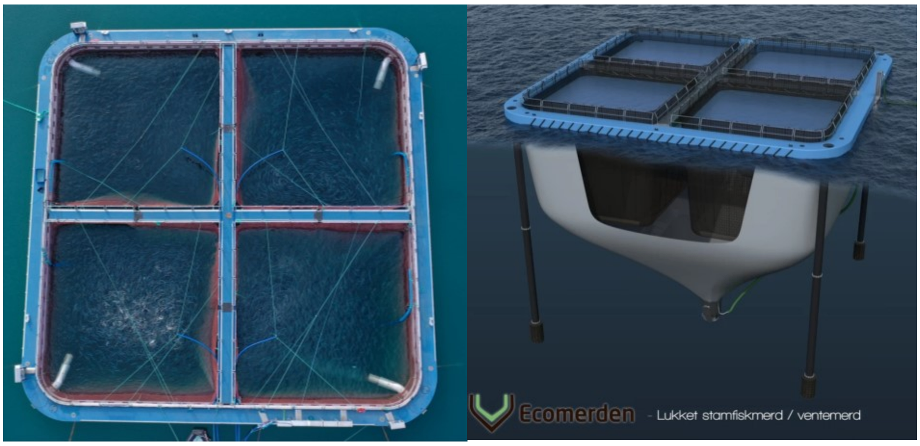

Note. A flexible closed bag is used to separate the fish from the external environment and water is collected far away from the water surface.
Source. (Ecomerden AS, 2020)

Figure 3. The FishGLOBE (left) and the Egget (right).

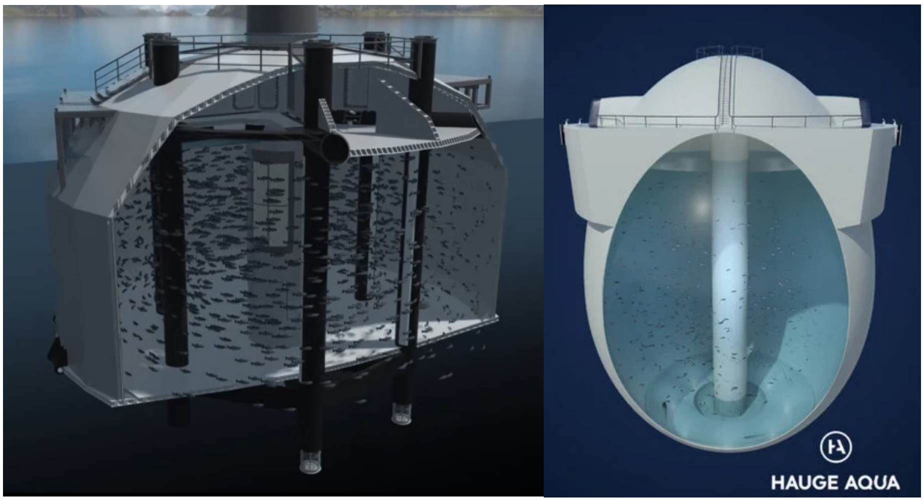

Note. These two solutions are fully closed cages where the fish are effectively separated from the external environment.
Sources. (FishGLOBE AS, 2020) (left), (Hauge Aqua AS, 2020)(right).

Computational fluid dynamics (CFD) is an interesting tool which can be used to model hydrodynamic systems, and aquaculture rearing systems are no exception. Relevant work on the field has been done by Rasmussen & McLean (2004), Gorle et al. (2018) and Behroozi & Couturier (2019), to cite a few examples. In contrast with model-size experimental campaigns, CFD models offer high flexibility, reduced costs and response times and can be used to model real-size cases without the scaling issues associated with experimental results. Nevertheless, CFD modelling requires a good understanding of the tools at hand and of their limitations, requiring validation and a good understanding of the physics at play.

Circular tanks with a tangential inlet and a central bottom outlet, widely used in land-based installations, are perhaps the simplest embodiment of rotating-flow closed rearing systems. This work concentrates on describing and subsequently modelling the hydrodynamics inside these systems as there is a good knowledge basis of practical information, experimental and numerical data available. CCSs share many similarities with land-based installations, and many lessons can be learned from the work done in this field. Nevertheless, economies of scale are pushing companies to design larger structures – both land and sea based – and there is little empirical information on the hydrodynamics of such structures. Studying, understanding, identifying and being able to model the main flow characteristics found in small size tanks is the cornerstone for understanding, designing and modelling more complex systems –tanks of different sizes and geometries with multiple inlets and outlets – such as floating CCSs and land-based recirculating aquaculture systems (RAS).

The main purpose of this work has been the implementation and validation of a CFD (OpenFOAM) model to represent the hydrodynamics inside circular aquaculture tanks with a diameter of 1.5 m. Subsequently, the validated modelling procedure was applied to tanks with diameters ranging from 5 to 40 m. It was found that when using the realizable $k-\varepsilon$ RANS turbulence model, the most important flow characteristics – a forced and a bathtub vortex – are successfully modelled in tanks with a diameter of up to 10 m. Results suggest that in larger structures, higher turbulence levels result in the dissipation of the bathtub vortex.

Chapter 2 presents the theoretical framework, introducing fish health parameters, closed fish rearing systems, tank hydrodynamics and important operational parameters.

Chapter 3 presents the specific objectives and methodology used, where the studied cases, the CFD modelling approach and setup are presented.

Chapter 4 presents the results for the model validation work and its subsequent implementation on larger structures.

Chapter 5 presents the conclusions and future work.

2. Theoretical framework

The starting point of this chapter is a brief section on Atlantic salmon health parameters followed by an introduction on closed rearing systems. The next section introduces tank hydrodynamics and the last section is dedicated to some important operational parameters.

2.1. Atlantic salmon health parameters in closed rearing systems

Appropriate rearing conditions are defined by fish health parameters. This section gives a brief overview of the most important parameters, which are dissolved oxygen (DO) concentration, fish metabolites and appropriate swimming speeds (this last point is central in this work).

According to Dalsgaard et al. (2013) DO concentration should be of 10 mg/L for Atlantic salmon smolt. DO concentration is related to oxygen consumption, which depends on many factors such as fish size, stocking density and activity. According to Thorarensen & Farrell (2011), 85%-120% oxygen saturation is necessary to maintain maximum growth rate for post-smolt salmon, with fish health compromised at values above 140%.

The concentration of fish metabolites must be kept below prescribed limits. CO_2 should be in the range between 10-12 mg/L (Mota et al., 2019; Thorarensen & Farrell, 2011) and total ammonia nitrogen (TAN) values should not exceed values of 0.01-0.2 mg/L (Bergheim et al., 2009; Thorarensen & Farrell, 2011).

Optimal swimming speeds for salmon rearing are well documented (Nilsen et al., 2019; Summerfelt et al., 2016), and there is a general consensus that the optimal swimming velocities lie in the range of 1-1.5 body lengths per second (BL s^{-1}). Solstrom et al. (2015) found that too high velocities will stress fish and negatively affect the growth rate, with best fish welfare found at 0.8 BL s^{-1}. Remen et al. (2016) found critical swimming speeds with values greater than 2 BL s^{-1}.

Optimal growing temperatures are at around 15-16°C (Koskela et al., 1997), although seasonal variations influence fish growth, independent of the size of the fish and the temperatures, with a possible link to photoperiod (Forsberg, 1995).

Fish stocking density is another important parameter, as it is correlated to oxygen consumption, metabolite production and fish interaction, which are also linked to the specific flow conditions inside the tank. These factors will determine local swimming velocities, fish schooling behaviour and metabolite and oxygen gradients and concentrations. Studies show that stocking densities of up to 75-80 kg m^{-3} of post-smolt Atlantic salmon (Calabrese et al., 2017; Thorarensen & Farrell, 2011) do not limit growth performance.

It is also interesting to make a note on the swimming behavior of Atlantic salmon as a function of the swimming speeds. Nilsen et al. (2019) found that moderate swimming speeds (0.36-0.63 BL s^{-1}) promote schooling behavior whereas low swimming speeds (0.10-.027 BL s^{-1}) resulted in random behavior. These observations were also confirmed by Rasmussen et al. (2005).

Table 1 shows a summary of the acceptable levels for water quality, density and flow parameters.

Table 1. Atlantic salmon health parameters.

Variable	Acceptable levels
Oxygen saturation	80-100%
CO_2	≤10 mgL^{-1}
NH_3	≤0.012 mgL^{-1}
NO_2	<0.1 mgL^{-1}
Density	≤80 kgm^{-3}
Water exchange in flow through systems	≥0.2-0.3 $Lmin^{-1}kg^{-1}$

Note. Acceptable levels for water quality, density and flow for maintaining growth and welfare of post-smolt Atlantic salmon.
Source. (Thorarensen & Farrell, 2011)

2.2. Closed fish rearing tanks

There are various solutions for recirculating closed rearing systems. The two main categories are raceway systems, in which fish are kept in a channel with a plug flow, and rotating flow systems, in which the fish swim around an axis. Mixed cell raceways are an interesting combination of these two, in which jet-induced vortices create adjacent rotating flow cells without the need to use separation walls.

In rotating-flow systems, the simplest embodiment is the circular tank with one tangential inlet and an outlet in the bottom centre. According to different authors (Almansa et al., 2014; Oca & Masalo, 2013; Timmons et al., 1998), these systems perform better in terms of homogeneity of metabolites and swimming velocities.

We can differentiate between land-based and floating systems. Land-based recirculating aquaculture systems (RAS) usually have a very small direct hydraulic connection of around 2% (J.M.R. Gorle, Terjesen, Mota, et al., 2018) and the rest of the water is treated and recirculated. In floating systems, at present day, the hydraulic connection is of 100%, as water is usually collected at depths of 20 m or more. There is good reason to believe that floating CCS will evolve into RAS systems to address the ever-pressing issue of environmental pollution.

2.3. Hydrodynamics in closed rearing systems

We will consider a circular tank with one tangential inlet at the wall and an outlet in the bottom centre. The combined effect of the water entering and leaving the tank generates a vortex. This vortical flow, which we will consider as the main flow structure (the azimuthal velocity component in cylindrical coordinates), can be subsequently subdivided into a forced vortex, generated by the inlet structure, and an irrotational vortex in the outlet area (under certain operational conditions), as described by various authors (Behroozi & Couturier, 2019; Despres & Couturier, 2006; J.M.R. Gorle, Terjesen, & Summerfelt, 2018; Oca & Masalo, 2013). The axial and radial velocity components account for the secondary flow structures, which are of particular importance in the boundary layers near solid walls and in secondary vortices in the bulk of the fluid.

2.3.1. Primary flow structures

A good introduction to the nature of the primary flow structures in fish rearing tanks can be made based on the finding of Yukimoto et al. (2010).

Figure 4. Experimental setup.

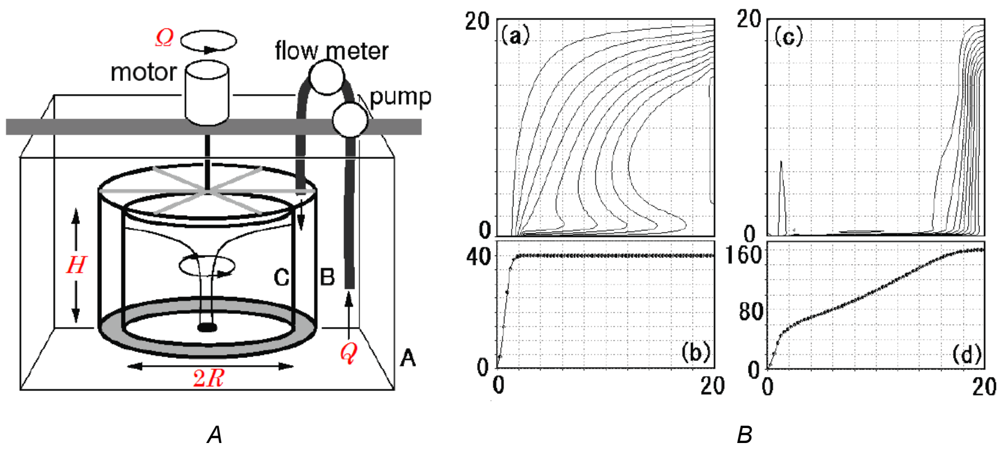

Note. A: Experimental setup to generate a bathtub vortex. B: Streamlines in the $r-z$ plane (a, c) and radial profiles of angular momentum at the mid-depth (b, d). Flow regime 1, irrotational vortex (a, b) and flow regime 2, forced vortex (c, d). *Source*. (Yukimoto et al., 2010)

Let us consider the angular momentum per unit mass, β:

$$\beta = Vr \tag{1}$$

Where r is the radial position. Considering solid-body rotation where $V = \Omega r$ (and where Ω is a constant angular velocity), β increases proportional to the radius squared.

The setup presented in Figure 5A consists of a cylindrical tank rotating at a constant angular velocity Ω, where a volume rate Q of water is drained through an outlet hole in the bottom centre of the tank and then reintegrated in order to keep the water level constant, two different flow regimes can be identified.

In flow regime 1, when Q is high and Ω is low, β is constant outside the core of the vortex, indicating the presence of an irrotational vortex (Figure 5A, a and b). In flow regime 2, in which Q is low and Ω is high, the angular momentum increases with the radius, and we are in the presence of a forced vortex (Figure 5A, c and d). These findings have been experimentally confirmed by Oca & Masaló (2013) and Masaló & Oca (2016) for impulse-force generated forced vortices.

In circular tanks, depending on the geometry, inlet-outlet configuration and on the value of Q, we can find ourselves in regime 1, regime 2 or a combination of the two.

2.3.1.1. *The forced vortex*

In circular culture tanks the water entering the fluid domain through the inlet applies a torque that forces the liquid to rotate like a solid body. The velocity at the walls is zero and boundary layers with shearing forces are created (Behroozi & Couturier, 2019) (in contrast with the solid body rotation case presented above, where there are no shearing forces at the walls). As we will see later, the boundary layers have a very important role in the hydrodynamics of these systems.

The resultant radial distribution of the tangential velocity components is very similar to the one presented in Figure 5Bd. Andersen et al. (2006) and Plew et. al (2015), among others, demonstrated experimentally that the axial distribution of the tangential velocity components is constant at each radial position.

2.3.1.2. *The irrotational vortex*

The irrotational vortex is also referred to as the "bathtub" vortex in free surface flows. As already hinted, the existence of an irrotational vortex at the outlet depends on the volumetric flow rate Q being discharged. According to Kawakubo et al. (1978), Q must exceed a threshold value Q_c, in agreement with the findings of Yukimoto et al. (2010). In other words, "as more water flows radially towards the tank centre, the conservation of angular momentum starts to predominate over tangential shear stresses and a free vortex forms" (Behroozi & Couturier, 2019).

Two well-known approximations of the velocities distribution in irrotational vortices are the Rankine combined vortex (Rankine & Roberts, 1858) and the Burgers vortex (Burgers, 1948). Taking Figure 5 as a reference, we can define two zones: a forced vortex[1] ($r < r_c$) zone and an irrotational vortex zone ($r > r_c$). The tangential velocities distribution according to Burgers' model is:

$$V = \frac{C}{r}\left(1 - e^{-\frac{ar^2}{2\nu}}\right) \tag{2}$$

Where ν is the kinematic viscosity of the fluid and a the strength of suction.

Figure 5c shows that the distribution of β matches the one described in regime 1 by Yukimoto et al. (2010) in Figure 5Bb.

Figure 5. Burgers and Rankine vortices velocities and momentum distributions

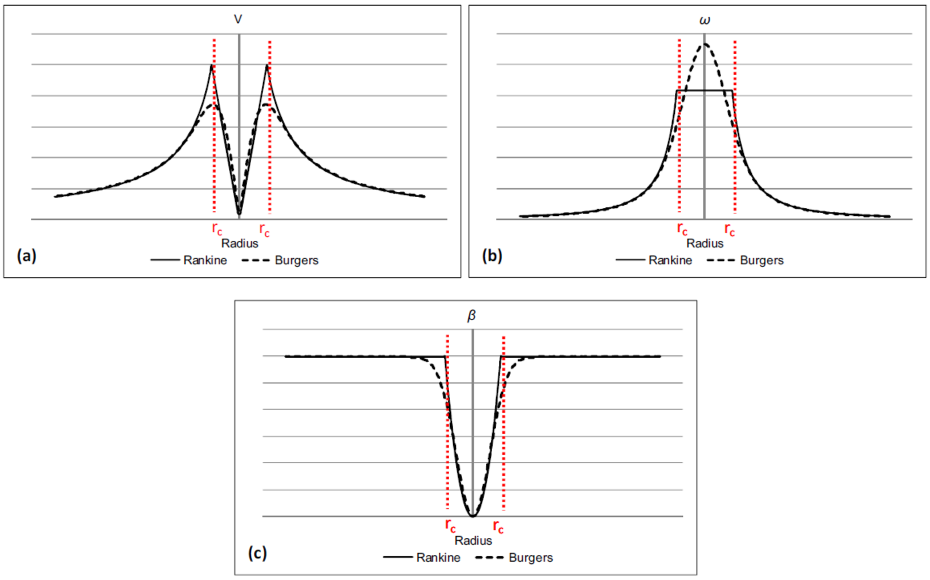

Note. Distribution of (a) tangential velocities V, (b) angular velocities ω and (c) angular momentum per unit mass β for the Rankine combined vortex (continuous line) and the Burgers model (dashed line). The vertical dashed line (red) indicates the distance from the water outlet where the forced vortex ($r < r_c$) is observed.
Source. (Masaló & Oca, 2016)

From a momentum conservation perspective, there is no energy consumption from an external source and no external torque is applied, so for an inviscid fluid β must remain constant along the radius. Contemporarily, the tangential velocity is inversely proportional to the radial position (Oca & Masalo, 2013), as Figure 5

[1] This forced vortex should not be confused with the forced vortex generated by an impulse force in the outer radii of the tank.

shows. Viscosity produces friction losses (proportional to squared velocities) which are not negligible near the rotation axis (Oca & Masalo, 2013), resulting in the Burgers and Rankine profiles previously mentioned.

2.3.2. Secondary flow structures

As already mentioned, the secondary flow structures are composed by the axial and radial velocity components. The secondary flow is primarily responsible for the mass flow towards the bottom outlet and mixing inside the tank. Mixing is very important as it will determine or hinder the existence of “dead” areas inside the tank, characterized by very low velocities, low DO concentrations and high metabolite gradients.

Let us consider the simplified case of a tank with a spinning cover and no inlets and outlets, as studied by Behroozi & Couturier (2019), where a forced vortex is generated. The resulting flow structures will be like the ones presented in Figure 6. In the boundary layer adjacent to the spinning cover, water moves towards the outer radius. In the boundary layer at the lateral wall, water moves downwards and in the boundary layer at the floor the water moves radially towards the centre, to move up again towards the top in the middle of the tank. In a simulated case Behroozi & Couturier (2019) reported very small radial and axial velocities in the bulk of the fluid. When considering an inlet and an outlet, if we find ourselves in this flow regime, most of the radial transport will happen exclusively through the boundary layers with very little mixing, especially in the middle of the tank.

Figure 6. Secondary radial flow in a tank.

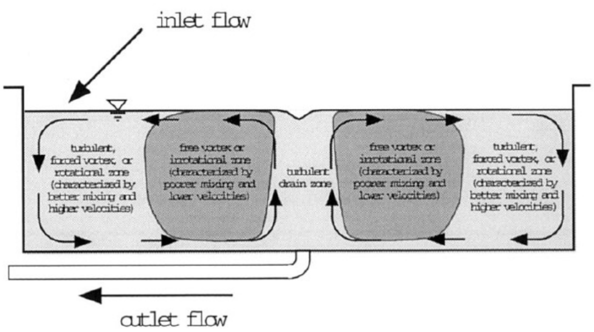

Note. Secondary radial flow created in a tank with a spinning cover.
Source. (Timmons et al., 1998)

The concept presented above is also confirmed by the findings of Yukimoto et al. (2010). Figure 5Bc shows the streamlines in a forced vortex flow where most of the flux is transported through the boundary layers in the wall and the floor (note the increase of β with radius in Figure 5Bd).

Figure 5Ba, on the other hand, shows the secondary flow streamlines in the case of an irrotational vortex, where there is radial flow towards the outlet in the bulk of the fluid at all radial positions, resulting in more intense mixing. These observations are pertinent in the case of small geometries like the setup presented in the figure. In larger geometries, turbulence levels increase and can strongly affect the resulting flow regime and secondary flow structures.

The boundary layer is responsible for the transfer of momentum between the walls and the bulk of the fluid. The thickness of the boundary layer, which is a function of the local flow velocity, the surface roughness and the turbulence intensity inside the tank, will strongly affect the resulting primary and secondary flow structures. More details on this are given in chapter 2.4.6 in relation to the effect of fish.

The effect of the free surface may also have an impact of the flow structure, especially in the presence of high flow rates and strong free surface deformations. Gorle et al. (2018) mention, for example, strong fluctuations of velocity measurements near the free surface in the centre of the tank. As Behroozi & Couturier (2019) note, the deformation of the water surface (generated by the forced and irrotational vortices) produces a pressure gradient along the bottom radius which enhances the boundary layer transport along the bottom.

2.4. Operational parameters and considerations

2.4.1. Introduction

What defines sound hydrodynamic properties inside a fish rearing tank? The optimization of fish growth parameters is a resource-intensive multidisciplinary field of study. A myriad of factors can influence the growth of fish, ranging from optimal swimming velocities, feed quality and tank hydrodynamics to light exposure and stress to name a few. Even the impact of tank colour has been documented (McLean et al., 2008). Moreover, seasonal variations are embedded into the life cycle of fish, which are growing with time, meaning that optimal growing conditions are dynamically changing. Thus, a rearing unit should have operational flexibility and the hydrodynamic performance of the tank should be optimized, or at least "mapped", for a range of possible operational conditions.

Let us consider the tank carrying capacity (Colt & Watten, 1988) which we can define as the maximum stocking density of fish which can be reared in a tank. Optimal and homogeneous dissolved oxygen and metabolite concentrations, swimming speeds and fish distribution are all a prerequisite to optimize the use of the available volume. Nevertheless, optimal rearing conditions vary throughout the life cycle of fish. As fish grow, the average swimming speed inside the tank must increase to fulfil the BL s^{-1} requirements and to compensate for the higher dissipation rates produced by the higher stocking densities (see chapter 2.4.6).

The maximum stocking density, which defines the maximum carrying capacity of the tank, is a function of the maximum size which the fish will reach inside the tank at the end of the rearing cycle. This tells us that the rearing conditions inside the tank are a function of the number of fish present inside the tank and of the specific life cycle period that the fish spend in it. We can thus conclude that the rearing tank should be designed to cover a specific period of the fish life cycle with a clearly defined final (maximum) stocking density.

Other operational considerations that affect the tank design are related to handling operations such as the removal of dead fish and grading and harvesting operations.

In the following sections, design and operational parameters which affect the hydrodynamics inside fish rearing tanks are presented.

2.4.2. Hydraulic retention time (HRT)

The hydraulic retention time (HRT) is the mean residence time the water spends inside the tank volume. It is a useful parameter to take into consideration, as it englobes the tank size and the volumetric flow rate. The HRT is defined as:

$$HRT = \frac{V}{Q} \tag{3}$$

Where V is the tank volume and Q is the volumetric flow rate.

According to a survey carried out by Summerfelt et al. (2016), for tanks built after 2013 with volumes between 653 and 21000 m^3, operational HRT values ranging between 34.8 to 52.5 minutes. Tanks in operation before 2010 have higher HRT values, ranging between 67 and 170 minutes. Considering a constant volume, there is a trend to increase Q, resulting in faster water exchange ratios and better water quality.

The dimensions and the proportions of the tank will influence the hydrodynamics. In cylindrical tanks the volume is a function of the diameter, D, and the water column height, H. Bigger tank sizes result in higher Reynolds numbers and in higher turbulence intensities. The tank geometry will also influence the pumping power necessary at the inlet structure and the settled solids management.

With respect to scaling effects, according to Føre et al. (2018), lower D/H ratios (deeper tanks) help to improve feed ingestion, but at constant D, increasing the depth will increase the volume and will result in an increase in HRT, which can impact negatively on the water quality. A bigger volume can also result in the existence of more "dead" areas and recirculation zones with poor water quality.

2.4.3. Mean swimming velocities

If we consider the size of salmon to range from 10 cm (smolt) to 75 cm (post-smolt), the range of swimming velocities inside the tank should be between 8 cm/s and 113 cm/s. Fish swimming behaviour is determined by the tangential velocity components in the tank, and for this reason different authors have proposed models to describe velocity distribution inside circular tanks (Behroozi & Couturier, 2019; Masaló & Oca, 2016; Oca & Masalo, 2013).

Oca & Masaló (2013) proposed a model that describes the radial distribution of the tangential velocities, V_θ in a circular tank without fish, which takes into consideration the flow regimes presented in chapter 2.3. The model is the following:

$$V_\theta = \frac{1}{r}\beta_0^{1-\frac{r}{R}}\beta_w^{\frac{r}{R}} \tag{4}$$

Where the angular momentum per unit mass near the tank wall, β_w, is:

$$\beta_w = m\sqrt{\frac{F_i}{H}} \tag{5}$$

Where F_i is the inlet impulse force.

The inlet impulse force F_i, as defined by (Tvinnereim & Skybakmoen, 1989), is :

$$F_i = \rho Q(V_{in} - V_1) \tag{6}$$

where ρ is the water density, Q the injected water flow rate, V_{in} the inlet jet velocity and V_1 the circulating velocity of the water tank.

The angular momentum per unit mass in the tank center, β_0, is:

$$\beta_0 = n(Q - Q_0) \tag{7}$$

Where $Q_0 = \frac{p}{n}$ represents the threshold value needed for the formation of the irrotational vortex, which is the same as Q_c (chapter 2.3.1.2). m, n and p are values determined experimentally by linear regression.

This model can be used to predict tank-specific velocity distributions with limited experimental or simulation campaigns.

We can see from expressions (5) – which defines the momentum distribution in a forced vortex – and (7) – which defines the momentum distribution in a bathtub vortex – that the impulse force, F_i, and the volumetric flow rate, Q, are key variables that define the velocity distribution. F_i is defined by the inlet structure and Q by the outlet structure.

2.4.4. Torque balance

If we consider momentum conservation inside a circular tank, the resultant torque applied on the system must equal zero, and therefore the input torque, T_i, must be equal to a resistance torque, T_r, which is produced by the shearing forces in the boundary layers at the walls. For a circular tank, we must consider the lateral walls, the floor and any structure protruding into the fluid domain (inlet and outlet systems, dead fish collection systems, etc.).

We can thus write a torque balance equation as:

$$T_i = T_{r,w} + T_{r,f} + T_{r,s} \tag{8}$$

Where $T_{r,w}$ is the resistance torque at the walls, $T_{r,f}$ is the resistance torque at the floor and $T_{r,s}$ is the resistance torque generated by any other structure.

Following the work of Oca & Masaló (2013), considering an inlet at the outer radius R, we start by defining the resulting input torque as:

$$T_i = F_i R = \rho Q (V_{in} - V_1) R \tag{9}$$

If we consider $V_{in} \gg V_1$, expressions (6) and (9) can be rewritten as:

$$F_i = \rho Q V_{in} \tag{10}$$

$$T_i = F_i R = \rho Q V_{in} R \tag{11}$$

The general expression for the resistance torque is:

$$T_r = \tau_0 A r \tag{12}$$

Where τ_0 is the average boundary shear stress in the surface area A, positioned at a distance r from the central axis.

For the circular tank we can write the following expressions:

$$T_{r,w} = \tau_0 A_w R \quad (13)$$

$$T_{r,f} = \int_0^R \tau_0 2\pi r^2 dr \quad (14)$$

In (Plew et al., 2015), a slightly different approach is used to determine the resistance torques, where:

$$\tau_0 = \rho C_d V_\theta^2 \quad (15)$$

Here, the friction coefficient, C_d, relates the boundary shear stress at the walls to the velocity squared. We can thus rewrite equations (13) and (14) as:

$$T_{r,w} = \rho C_{d,w} V_{\theta,w}^2 A_w R \quad (16)$$

$$T_{r,f} = \int_0^R \rho C_{d,f} V^2 2\pi r^2 dr \quad (17)$$

Where $V_{\theta,w}$ is the tangential velocity at the wall, $C_{d,w}$ is the drag coefficient of the wall and $C_{d,f}$ is the drag coefficient of the floor.

It is worth noting that when looking at the boundary layer, the wall shear stress, τ_w, is:

$$\tau_w = \mu \left(\frac{\partial u}{\partial y}\right)_{y=0} \quad (18)$$

Where μ is the dynamic viscosity, u the flow velocity parallel to the wall and$y$ the normal distance to the wall.

If we considered the presence of a vertical pipe, for example, as the inlet structure, we can follow the procedure of Behroozi & Couturier (2019) and approximate the drag force exerted on the pipe as that for flow over cylinders, and the torque applied on this structure results as:

$$T_{r,s} = \frac{\rho V_{\theta,s}^2}{2} C_{d,s} A_p r_s \quad (19)$$

Where $V_{\theta,s}$ is the tangential velocity at the radial position r_s where the vertical pipe is located and $C_{d,s}$ is the drag coefficient of the pipe (which is a function of the Reynolds number which is a function of the diameter of the pipe).

Equation (8) is useful to evaluate the impact of the tank walls and any other structure present inside the tank.

2.4.5. Tank resistance coefficient

Oca & Masaló (2007) derived an experimental determination of the tank resistance coefficient, C_t:

$$C_t = \frac{2QV_{in}}{AV_1^2} \tag{20}$$

where A is the wet area.

For the derivation of this expression a fully turbulent flow is considered, that is, $Re{\sim}10^6$. C_t allows to to estimate the the average velocities inside a tank as a function of Q and V_{in}, assuming $V_{in} \gg V_1$, and to evaluate the energy required to achieve predetermined average velocities (Oca & Masalo, 2013).

This parameter, as well as the torque balance approach, is of particular interest when having experimental or numerical data at hand, as it can be used to evaluate the resistance coefficient of the tank as a function of the resultant mean velocity, V_1, but also as a function of different operational parameters (geometry, specific configurations, surface roughness, in the presence of fish, etc.).

Combining expressions (10) and (20) we can determine the relationship between the impulse force F_i and the average tangential speed V_1:

$$V_1 = \sqrt{\frac{2}{\rho AC_t}}\sqrt{F_i} \tag{21}$$

Where the average velocity is proportional to the square root of the impulse force, as also expressed in equation (5).

2.4.6. On the presence of fish

The effect of fish on the hydrodynamics of aquaculture tanks has been documented by some authors (Almansa et al., 2014; J.M.R. Gorle, Terjesen, Mota, et al., 2018; Masaló & Oca, 2016; Plew et al., 2015; Rasmussen et al., 2005). The presence of fish reduces the tangential velocity components and can result in the elimination of the bathtub vortex – as documented by Almansa et al. (2014) and Masaló & Oca (2016) – in small tanks. Other direct consequences are an increase in the tank resistance coefficient, C_t, (Masaló & Oca, 2016; Plew et al., 2015), higher turbulence levels and enhanced mixing (Rasmussen et al., 2005).

An increase in C_t should not be interpreted as fish taking part in the torque balance in equation (8). When the swimming speeds promote schooling behaviour, it has been observed that fish tend to keep their position in the tank (Duarte et al., 2011; Nilsen et al., 2019): fish use energy to overcome their own body drag, so we could say that fish have their own torque balance equation.

Fish swimming activity does impact the torque balance, but through a different mechanism. As it has already been mentioned, fish enhance mixing. This is due to the wakes and vortices introduced by fish swimming activity. Enhanced mixing is also a synonym of higher levels of turbulence, which result in more efficient momentum transport towards the boundary layers and an increase of the apparent effective roughness of the tank walls (Plew et al., 2015), which translates in a thickening of the boundary layer, which in turn is responsible for the reduction of the tangential velocities.

The impact of fish on a specific tank configuration is a function of the stocking density and fish size. Plew et al. (2015) evaluated the impact of different fish stocking densities (ranging from 15.3 to 79.4 kg m^{-3}). The presence of fish resulted in higher dissipation rates and higher stocking densities resulted in lower velocities and higher values of C_t. It was also found that tank occupation could be measured via the turbulent kinetic energy and that it varied with different stocking densities.

From a practical point of view, when evaluating the hydrodynamics in culture tanks, the presence of fish will result in higher energy requirements to obtain the desired swimming velocities. Nevertheless, it is difficult to evaluate a priori to what extent the presence of fish will modify the resulting tangential, radial and axial velocity distributions. Enhanced mixing will contribute to the reduction of gradients (velocity, DO and metabolites) and dead areas inside the tank and will promote the resuspension of solids.

2.4.7. Inlet structures

From equation (6) we know that the impulse force, F_i, is a function of the inlet velocity, V_{in}. For a constant volumetric flow rate Q, the inlet velocity can be modified through the inlet area. The power input, P_i, is (Papáček et al., 2019):

$$P_i = \frac{1}{2}\rho V_{in}^2 Q \tag{22}$$

In which $Q = V_{in}A_{in}$, so we can write:

$$P_i = \frac{1}{2}\rho V_{in}^3 A_{in} \tag{23}$$

Behroozi & Couturier (2019) mention a value of around 8.5/1 to minimize P_i, which is related to minimizing the values of the resistance torque at the tank surfaces.

Different authors have studied inlet configurations in culture tanks (Burley & Klapsis, 1985; Davidson & Summerfelt, 2004; J.M.R. Gorle, Terjesen, & Summerfelt, 2018; Odeh et al., 2004; Tvinnereim & Skybakmoen, 1989). The number of inlets, the injection angle and the radial and axial positions will affect the resulting hydrodynamics.

Burley & Klapsis (1985) report optimal injection angles between 25 and 30° in order to avoid jet impingement against the side walls, which was observed when the orientation angle was 0°(flow parallel to the wall). Davidson & Summerfelt (2004) found that the orientation of the inlets affected the mixing inside the tank, and proposed multiple inlets with various orientations, including inlets heading radially inwards (90° angle) near the tank bottom. Gorle et al. (2018), (2019) studied different inlets configurations, including V-nozzles placed in intermediate radial positions, and found that smaller multiple jets organize better with the mean flow.

2.4.8. Outlet structures

Up to this point we have considered a single outlet at the bottom centre of the tank. In practice, the following outlet structures are used:

i) Single outlet in the bottom centre of the tank.

ii) Double outlet split between outlets placed in the centre bottom and the tank wall (Cornell type).

iii) Double outlet split between outlets placed in the centre, in the bottom and at a secondary upper position.

iv) A triple-drain outlet system in which the wall outlet and the two central outlets are used.

A key concept in multi-outlet arrangements is the flow-split between the different outlets. When using a wall outlet, part of the inlet flow is short-circuited. The advantage with this type of construction is that by regulating the flow-split, the intensity of the irrotational vortex at the tank centre can be controlled (Despres & Couturier, 2006). In other words, we can regulate the value of Q in equation (7) and modify the value of the angular momentum at the tank centre. From a practical point of view, modifying the strength of the irrotational vortex can be used to modify the resulting tangential velocities profile along the tank radius. Interestingly enough, the intensity of the irrotational vortex is a function of the flow split between the centre and lateral outlets, and not of the flow split between the bottom and top outlets at the centre (Despres & Couturier, 2006).

A secondary outlet in the centre above the bottom drain can lead to the resuspension of settled solids, which can be solved, for example, by using a bell-mouthed standpipe outlet, as noted by Burley & Klapsis (1985), although this is very punctual solution.

2.4.9. Solids management

From an operational point of view, a tank should be self-cleaning, that means, it should be able to concentrate and flush settleable solids. The effective removal of solid wastes (fish faeces, uneaten feed) is important in order to guarantee good water quality. Nevertheless, most of the solids found in culture tanks are suspended solids with diameters of less than 20 μm and a specific gravity very similar to that of water (Chen et al., 1993). Good mixing will guarantee the entrainment of these suspended solids towards the outlet. On the other hand, dead zones and recirculation zones will hinder their flushing.

Depending on the flow regime, settleable particles will settle in the bottom or will be resuspended. When particles settle, the secondary radial flow towards the outlet in the boundary layer should be strong enough to carry with it the settles particles towards the outlet. This is the so called "tea-cup effect". These tanks can operate as continuous or intermittent separators, depending on the flushing mechanism. The peculiarities of different removal mechanisms was summarized by Timmons et al. (1998). Authors often make reference to the D/H ratio (which for land based circular tanks is in the range of 1/5 to 10/1) in relation to the ability of the tank to flush settleable solids (Burrows & Chenowith, 1955; Despres & Couturier, 2006; Larmoyeux et al., 1973).

In the presence of high fish stocking densities, and in flow regimes with small HRT values, settleable particles will tend to be resuspended and carried away by the main flow in the bulk of the fluid together with the suspended solids. In a CFD analysis of an ellipsoidal culture tank in which aquaculture-like particles with diameters between 1-3000 μm were simulated, Klebert et al. (2013) found that almost all of the particles were removed after a maximum interval of two HRT cycles.

3. Specific objectives and methodology

3.1. Specific objectives

The specific objectives of the present work are:

1. The main purpose of this work is the implementation and validation of a CFD (OpenFOAM) model to represent the hydrodynamics inside circular aquaculture tanks with a 1.5 m diameter documented by Oca & Masaló (2013).
2. Evaluate the performance of different turbulence models, for both high-Re and low-Re numbers, as the conclusions drawn from the literature are conflicting. Importance is given to the generation of the bathtub vortex in the outlet area.
3. Evaluate if a variation of the inlet turbulence properties – as a simplified method to account for enhanced mixing, emulating the presence of fish – will affect the resulting flow.
4. Apply the tested modelling approach to tanks with diameters between 5 m and 40 m and evaluate the scaling effect on the tank hydrodynamics.

3.2. Methodology

The validation work is based on published experimental data, the reference setup being the one presented in (Oca & Masalo, 2013), in which a circular tank with a tangential inlet is subjected to different flow rates in two diameter-to-depth configurations. The presence of an irrotational vortex in the outlet section in specific flow conditions was of central interest in this phase. The reason for this is that, as already mentioned in section 2.3, the two most distinct characteristics of the flow inside closed circular systems are the forced vortex produced by the inlet system, and in certain flow regimes, the bathtub vortex which forms in the outlet region. The presence of this vortex can strongly influence the velocity profiles inside the tank, and for this reason it is essential to model it.

The first step, which is summarized in the previous chapter, consisted in carrying out a literary review with various parallel goals: to define important operational and fish health parameters in closed rearing systems and to have a general understanding – from a practical, theoretical and experimental point of view – of the hydrodynamics and main flow characteristics inside these systems, in relation to different operational parameters and configurations.

The next step consisted in modelling the experimental setup mentioned previously in order to define the most important modelling parameters, such as an appropriate turbulence model capable of capturing the main flow properties, the type of near-wall treatment and the mesh quality. Finally, the validated modelling procedure was applied to structures with diameters of up to 40 m.

3.2.1. CFD modelling and implementation

OpenFOAM (Weller et al., 1998) v7 was used to solve the Reynolds-averaged Navier-Stokes (RANS) equations with the volume of fluid (VOF) method on regular or irregular polyhedral meshes. The in-built solver used was simpleFoam, a RANS solver for incompressible steady-state flows. The semi-implicit method for pressure linked equations (SIMPLE) algorithm was used to solve the continuity and momentum equations.

3.2.2. Tank geometries and parameters

3.2.2.1. Validation cases

Figure 7 and Table 2 show the tank geometry and the operational setup modelled. The first validation step consisted in evaluating different turbulence models. Subsequently, with a defined turbulence model, the effect of the inlet turbulence intensity was evaluated. The Reynolds numbers, based on R, H and V_{in} are $Re_{R,V_{in}}$ = 1.85x10^6 and $Re_{H,V_{in}}$= 4.92 x 10^5.

Figure 7. Experimental setup.

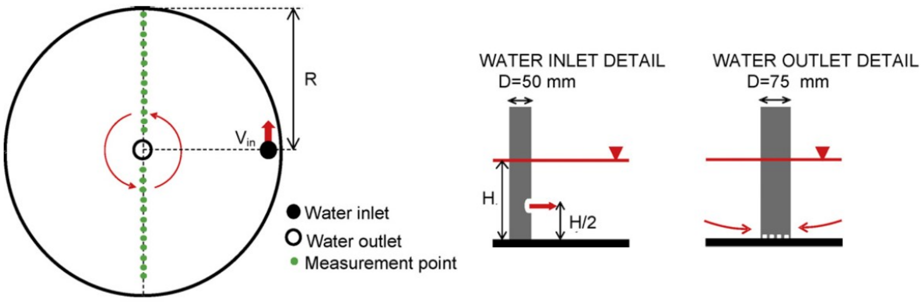

Note. Cylindrical tank experimental setup used in the validation cases. The green points represent the measuring positions at a depth of H/2. *Source*. (Oca & Masalo, 2013)

Table 2. Experimental 1.5 m tank setup configuration used to validate the model.

Case	Parameters					
	H (m)	$\frac{D}{H}$	Q (l/h)	V_{in} (m/s)	F_i (N)	Predominant regimes
V1	0.2	7.5:1	2200	2.5	1.47	1≫2

Note. Experimental tank configuration, data elaborated from (Oca & Masalo, 2013).

3.2.2.2. Prototype cases

For the prototype cases, five different geometries of different sizes were considered, with the scope of evaluating the scaling effect (schematically shown in Figure 8). They consist of four cylindrical tanks with the D/H=7.5 ratio (same as the validation case), with D values of 5 m, 10 m, 20 m and 40 m. The last geometry is an elliptical tank with D/H=1.25, in which the main dimension is the depth. It consists of a convex elliptic surface extending from $H/2$ down to the outlet. The inlet positioned at $H/4$ from the top. Further details are given in Table 3 and Table 4.

Figure 8. Proposed geometries

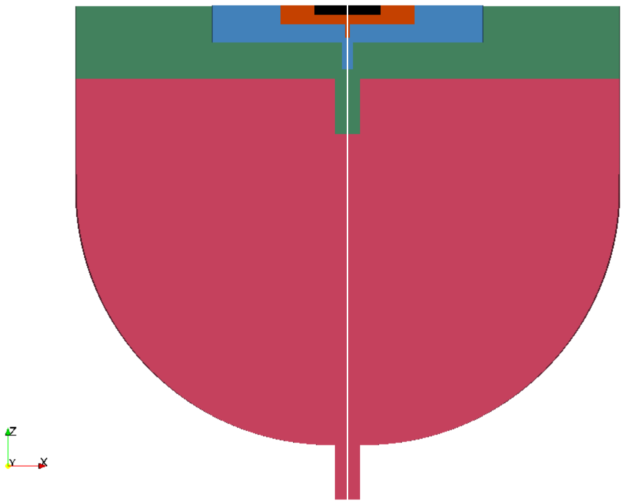

Note. Cylindrical tanks with D/H=7.5 and diameters ranging from 5 to 40 m and elliptical tank with D=40 m.

The dimensions in the first four cases have the exact same proportions, the same inlet velocities and the same HRT values. The last geometry was tested with three different operational setups, with higher HRT values, see Table 3.

Table 3. Prototype cases (D=40 m) setup configurations.

Case	Parameters								
	D (m)	H (m)	$\frac{D}{H}$	$Vol.$ (m^3)	Q (m^3/s)	V_{in} (m/s)	F_i (N)	HRT (min)	Further remarks
P1	5	0.7	7.5:1	13	0.009	2.0	18	25	Cylindrical
P2	10	1.3	7.5:1	105	0.07	2.0	139	25	Cylindrical
P3	20	2.7	7.5:1	837	0.6	2.0	1123	25	Cylindrical
P4	40	5.3	7.5:1	6698	4.5	2.0	8956	25	Cylindrical
P5.1	40	32	~1.25:1	32751	6.7	0.5	3376	82	Elliptical
P5.2	40	32	~1.25:1	32751	3.4	0.25	844	160	Elliptical
P5.3	40	32	~1.25:1	32751	2.2	0.125	375	250	Elliptical

Note. Prototype configurations with different geometries and HRTs.

Table 4. Prototype cases (D=40 m) Re numbers.

Turbulence model	Reynolds numbers	
	$Re_{R,V_{in}}$	$Re_{H,V_{in}}$
P1	5,05E+06	1,35E+06
P2	1,00E+07	2,67E+06
P3	2,02E+07	5,38E+06
P4	4,02E+07	1,07E+07
P5.1	1,00E+07	1,61E+07
P5.2	5,14E+06	8,23E+06
P5.3	3,29E+06	5,27E+06

Note. Different Re values are obtained when considering different reference dimensions.

3.2.3. Mesh configurations

A similar approach to the one used by Behroozi & Couturier (2019) was used, in which symmetry of flow around the central axis was considered. Nevertheless, a 3D model was used. The domain was reduced to a sector of 2° to 12° with cyclic boundary conditions. Each sector was divided into 4 elements in the azimuthal direction, meaning that some degree of variation of the velocities in the tangential direction was allowed. To guarantee similar flow conditions between the 3D setup and the model, the inlet was subdivided into 180 or 30 smaller inlets. The volumetric flow rate at the inlet was set to 1/180 or 1/30 of the nominal value, with the same impulse force. Although the utilization of an array of inlet jets deviates from the original setup, using cyclic boundary conditions resulted in a drastic reduction of the total number of mesh cells with a consequent reduction in the computation time.

Table 5. Number of cells used in each case mesh.

Case	Number of cells			
	v0	v1	v2	v3
V1.1[2]	44700	-	-	-
V1.2[3]	18740	31320	69004	119184
P1	5320	19352	68472	-
P2	6132	19240	68996	-
P3	6108	19044	68432	-
P4	6060	18912	68048	-
P5	42076	71640	156632	-

Note. This table sums up the number of mesh refinement steps carried out in each case.

[2] Low-Re mesh

[3] High-Re mesh

Figure 9. Case V1.2 meshes (v1 and v3).

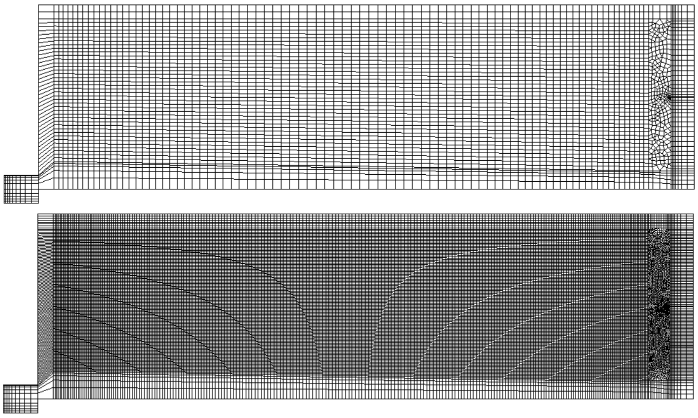

Note. High-Re mesh where the thickness of the first cells in the walls remains constant after refinement (case V1.2).

It must be noted that the use of cyclic boundary conditions is a simplification in which there is only one dimensional degree of freedom (in the z-direction) at the axis of rotation. This means that results obtained in the vicinity of the axis should be handled with care. In practice, a wall at a small distance from the axis, with zero gradient conditions, was used in all cases.

All meshes were made using Gmsh (Geuzaine & Remacle, 2009). Scripts were created in which the dimensions and the discretization could be easily modifiable. This proved particularly helpful when setting up multiple cases and when scaling geometries. The script used to generate the meshes for case P5 can be found in Appendix A.

Figure 10. High-Re and low-Re meshes and boundary layer discretization.

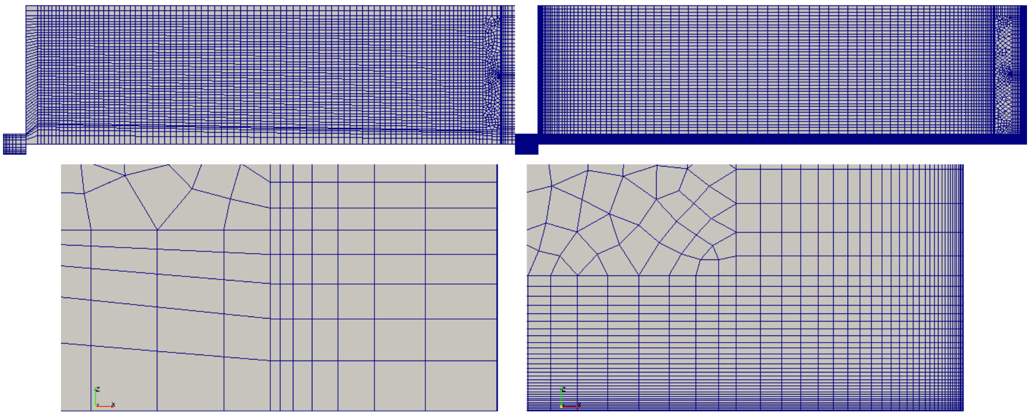

Note. In low-Re meshes (bottom right) the boundary layer must be discretized with 10-20 layers.

Figure 11. Case P5, mesh v0.

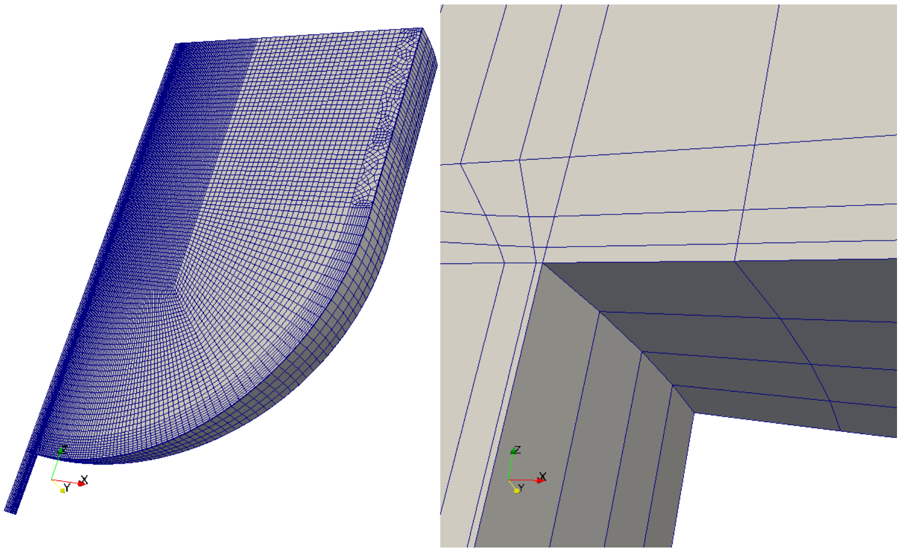

Note. Domain discretization of case P5. The boundary layer thickness (first cell) is kept constant when refining the mesh.

Particular attention was paid to the boundary layers, as the size of the first cell depends on the local flow conditions and the turbulence model used (more details are given in chapter 3.2.4). A summary of the number of elements used in the mesh refinement steps for the studied cases is given in Table 5. Note that case V1.1 refers to the low-Re turbulence models mesh and V1.2 to the high-Re turbulence model mesh. Some examples of meshes are shown in Figure 9, 10 and 11.

3.2.4. Turbulence models

The flow inside aquaculture tanks is turbulent (the bigger the dimensions, the more turbulent the flow is) and strongly vortical (Behroozi & Couturier, 2019). Different turbulence models have been used in the literature to model the hydrodynamics of these systems. These are the $k-\varepsilon$ model (Chun et al., 2018; Jeong et al., 2004; Rasmussen & McLean, 2004), the realizable $k-\varepsilon$ model (Jagan M.R. Gorle et al., 2018; J.M.R. Gorle et al., 2019), the $k-\omega$ SST model (Klebert et al., 2013; Papáček et al., 2019), the $k-kl-\omega$ model (Chun et al., 2018) and Reynolds stress models (RSM) (Behroozi & Couturier, 2019; Chun et al., 2018), among others. Some of the conclusions regarding the applicability of these models are contradicting. For instance, Behroozi & Couturier (2019) conclude that the RSM model is the most appropriate as it can model strong turbulence anisotropy, whereas Chun et al. (2018), when modelling MCRs, conclude that the RSM model does not succeed in modelling the expected vortices but the $k-kl-\omega$ yields better predictions.

The swirl number, S, which is the ratio of the axial flux of angular momentum to the axial flux of axial momentum is defined in (Behroozi & Couturier, 2019) as an indicator to select the type of turbulence model. According to these authors, for values of $S < 0.5$, of the above-mentioned models, the realizable $k-\varepsilon$ is a more appropriate selection, whereas for values of $S > 0.5$ the RSM model is more suitable.

In the present work, the following turbulence models were evaluated: realizable $k-\varepsilon$, SST $k-\omega$ and $k-kl-\omega$. The selection of these turbulence models was motivated by the following reasons.

1. Published results: the first and most important source of information were scientific articles in which many of the models used have already been evaluated to a certain extent.
2. Models compatible with the available hardware: due to limited computational resources, RSM models and large eddy simulations (LES) were not considered.
3. Boundary layer modelling: high and low Reynolds number turbulence models require different refinement strategies at the boundary layer and the need or not to use wall functions. Both modelling approaches were considered.

With the above premises, a summary of the models used is given in Table 6.

Table 6. Turbulence models used.

	Remarks	
Turbulence model	Re	Wall functions
realizable $k-\varepsilon$	High	Yes
SST $k-\omega$	Low	No
$k-kl-\omega$	Low	No

Note. Different turbulence models were used based on the literature and the modelling approach.

In low-Reynolds number turbulence models no wall functions are necessary and the mesh is required to resolve the viscous sub-layer with 10-20 layers. In these models the first cell must be placed within viscous sublayer at $y^+ < 5$, where y^+ is the dimensionless perpendicular distance from the wall. In high-Reynolds number turbulence modes wall functions are used, and the first cell next to the walls should be in the inertial sublayer, at $30 < y^+ < 200$ (Moukalled et al., 2016).

To achieve this, the following procedure was adopted:

1. Generation of an initial mesh, in which the boundary layers are independently defined. When defining the boundary layer, positions where maximum and minimum values of y^+ may occur shall be taken into consideration, as they will require the thinning or thickening of the first cell.
2. An initial case is computed until the tangential velocity profile at the mid-height stabilizes. Subsequently the value of y^+ is calculated, and based on the results, the boundary layer is modified (the first cell moved closer or farther away from the wall), and the mesh is regenerated.
3. Point 2 is repeated until satisfactory values of y^+ are achieved, and the main flow characteristics are identifiable. The final step is the refinement of the mesh (except the size of the boundary layer elements normal to the walls) with the goal of establishing mesh independence of the solution.

In general, it was much easier to generate the boundary layers for the low-Re meshes as only one or two regeneration steps are needed. For the high-Re meshes, the preparation work was more challenging. In regions of the fluid with low velocities the boundary layers in adjacent walls thicken; if we consider a case with a forced vortex, the boundary layers will the thinnest at the outer walls and the outer portions of the bottom surface, whereas close to the centre they will thicken, to thin down again at the outlet. In presence of a pure irrotational vortex the boundary layer is the thinnest in the centre of the tank and thickens proportionally to the tank radius.

3.2.5. Boundary conditions

The initial boundary conditions for the turbulent energy, k, the turbulent dissipation rate,ε, and the specific dissipation rate, ω, at the inlets were defined with the following equations:

$$k = \frac{3}{2}(UI)^2 \tag{24}$$

Where U is the inlet velocity and I is the turbulence intensity.

$$\varepsilon = C_\mu^{0.75}\frac{k^{1.5}}{l} \tag{25}$$

$$\omega = C_\mu^{-0.25}\frac{k^{0.5}}{l} \tag{26}$$

Where C_μ is a turbulence model constant which normally has the value 0.09 and l is the turbulent length scale, based on the mixing length.

The mixing length is defined as $l = 0.07d_h$, where d_h is the hydraulic diameter which was defined as the inlet height. The turbulence intensity was tested at 5%, 10%, 20% and 50% in case V1.2.

As a rule of thumb, for the initialization of the simulations, the internal domain values of k were set with the same value at the inlet, whilst the ε values were set at 1/4-1/17 of the inlet value. This setup produced smooth initializations in all simulations.

Figure 12. Cases setup.

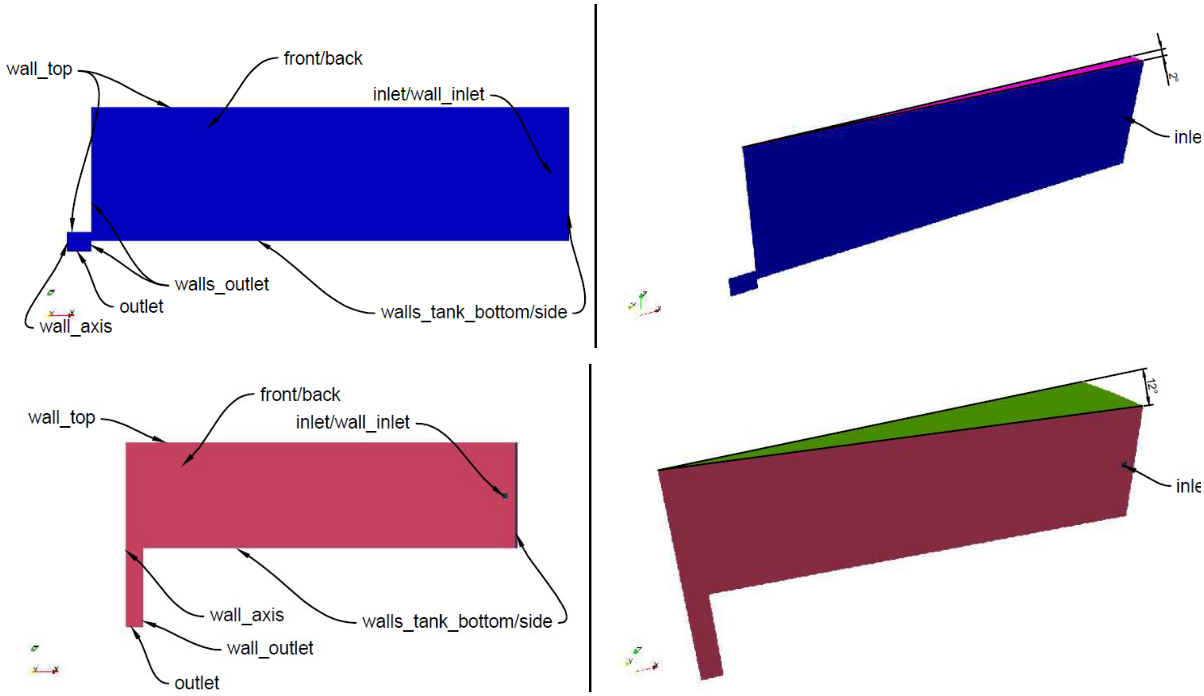

Note. Validation cases setup (top) and prototypes setup (bottom). Note the presence of a cylinder in the outlet region in the validation case.

Figure 12 presents the basic setups used in the different cases. In the validation setup a cylinder is placed at the tank centre. The flow is velocity-driven, in which a volumetric flow rate was defined at the inlet. The outlet velocity was defined with a zero gradient boundary condition for the velocity and a fixed value of zero pressure. In the prototype cases, backflow at the outlet was prohibited. Elements labelled "wall_" are walls with a slip condition and include the water surface. Cyclic conditions are assigned to the "front" and "back" boundaries. The definition of the walls with no slip boundary conditions ("walls_") is summed up in Table 7. The OpenFOAM boundary condition files for case P5.1 are found in Appendix B.

Table 7. Definition of the wall boundaries.

Variable	Turbulence model Realizable $k-\varepsilon$	SST $k-\omega$	$k-kl-\omega$
U	type noSlip;	type noSlip;	type noSlip;
p	type zeroGradient;	type zeroGradient;	type zeroGradient;
ν_T	type nutkWallFunction; value uniform 0;	type nutLowReWallFunction; value uniform 0;	type nutLowReWallFunction; value uniform 0;
k	type kqRWallFunction; value uniform 1e-12;	type fixedValue; value uniform 1e-12;	type fixedValue; value uniform 1e-12;
ε	type epsilonWallFunction; value uniform 1e-12;	-	-
ω	-	type omegaWallFunction; value uniform 1e-12;	type fixedValue; value uniform 1e-11;
kl	-	-	type fixedValue; value uniform 0;

Note. OpenFOAM nomenclature is used. Note how the last two columns describe low-Re wall treatment.

3.2.6. Numerical discretization and convergence criteria

A steady-state, second-order accurate and fully bounded setup was used. All of the convective terms, except for the velocity, were discretized using the Gauss scheme and the limited linear differencing total variation diminishing scheme (TDV) (first/second order bounded) interpolation scheme. The convective velocity term was discretized using the Gauss scheme and the linear upwind differencing interpolation scheme (first/second order, bounded).

The gradients were discretized with the second order Gaussian integration scheme, cell limited in all terms except for the velocity and pressure, where no gradient limiter was used. Linear interpolation (central differencing) was used.

The convergence criterion was set to residual values of 10^{-5} for the velocity components. This condition was seldom fulfilled in the presence of a bathtub vortex throughout the entire water column (in particular for the radial and axial velocity components), so the normal procedure was to reinitialize each case with a finer mesh and evaluate at the end of the run if the maximum values of V_θ changed considerably or not. It was observed that when the flow is dominated by a bathtub vortex, the system is dynamic and the residuals oscillate around relatively constant values. The torque equilibrium approach was used to check the solution once the tangential velocity profiles in the mid-height stabilized. For this purpose, the OpenFOAM built-in "wallShearStress" function object was used to extract the wall shear stress values at the walls.

The OpenFOAM fvSchemes and fvSolutions files can be found in Appendix C.

4. Results and discussion

In chapter 4.1 the results on the validation cases will be discussed and in chapter 4.1.4 the results on the prototype cases.

4.1. Validation cases

The results for the different turbulence models are presented first, followed by the impact of the inlet turbulence intensity on the tangential velocities distribution.

4.1.1. Turbulence models

Figure 13 shows the V_θ and β profiles obtained with the three turbulence models listed in Table 6. The three setups were done considering a 5% turbulence intensity in the inlet. As the results show, only the realizable $k-\varepsilon$ model can generate the forced and bathtub vortices inside the tank. The results obtained with this model overestimate slightly the experimental results. This can be in part due to the simplified cyclic setup, but also due to the mesh resolution inside the domain. The β profile connects the horizontal profile of the bathtub vortex with the forced vortex profile.

The SST $k-\omega$ model depicts the forced vortex quite well, but the bathtub vortex is completely damped. The $k-kl-\omega$ model produced a similar profile but overestimated the forced vortex. This last model was very sensible to the initial turbulence properties.

Figure 13. V_θ and β profiles with different turbulence models at H/2.

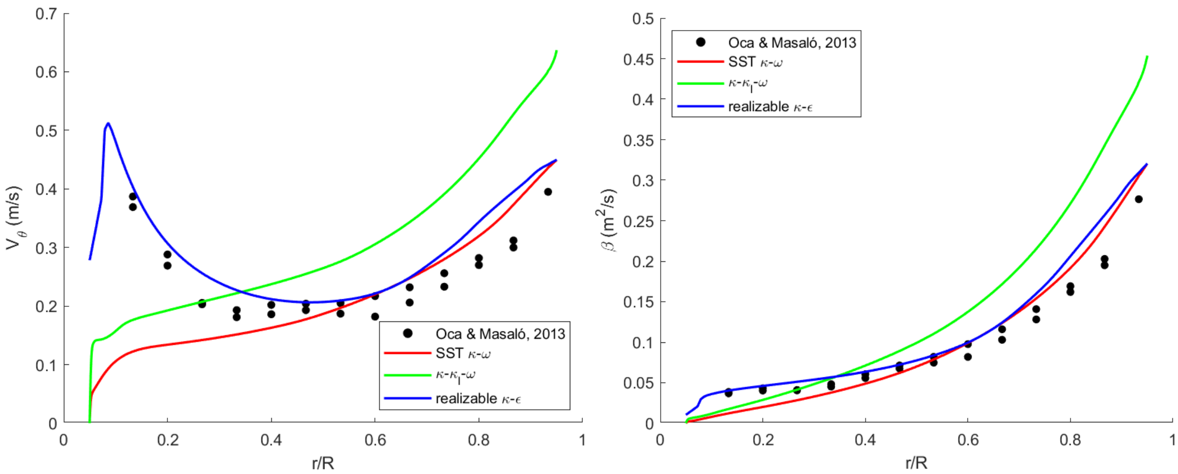

Note. Of the three turbulence models tested, only the realizable $k-\varepsilon$ model was capable of representing the bathtub vortex.

Figure 14 shows the radial velocity component V_r throughout the water column at R/2. In the bulk of the fluid, the radial velocity component is very small and it increases considerably in the boundary layer. Both the SST $k-\omega$ and $k-kl-\omega$

models give information of the velocities and thickness of the boundary layer, whereas the realizable $k-\varepsilon$ model does not. The results show that most of the radial flow occurs at the boundary layer or near the bottom surface.

Figure 14. V_r profiles with different turbulence models at R/2.

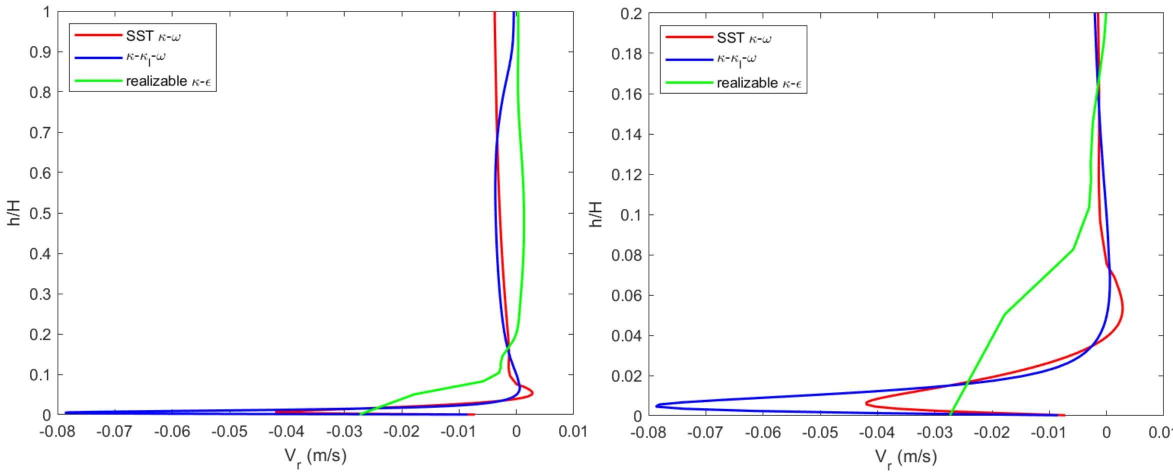

Note. The low-Re turbulence models give information on the flow and the thickness of the boundary layer whilst the realizable $k-\varepsilon$ model does not.

Figure 15 shows the turbulent kinetic energy k, distribution and Figure 16 the eddy viscosity ν_T, distribution. These figures help to understand the resulting velocity profiles. In both the SST $k-\omega$ and $k-kl-\omega$ models there are higher levels of turbulence, in particular in the vicinity of the outlet. It is worth noting that the k distribution between the SST $k-\omega$ and the realizable $k-\varepsilon$ models is not very different. k levels seem to be higher in the realizable $k-\varepsilon$ model case near the tank centre. The ν_T contours showr a different picture, in which the eddy viscosity levels are much higher in the two high-Re turbulence models. This may indicate that the free-vortex is being dissipated by an overestimation of ν_T, similar to the observations made by Plew et al. (2015) and Masaló & Oca (2016) on the effect fish can have in the smoothening of V_θ profiles.

Figure 17 shows snapshots of the secondary flow structures generated by the three different models. In the case of the SST $k-\omega$ and $k-kl-\omega$ models, in the presence of a forced vortex, most of the transport occurs through the boundary layer at the tank floor. We can see two secondary vortices forming next to the inlet, from which part of the flow moves towards the side wall, whilst most of the flow is transferred to the bottom boundary layer. The outlet appears to collect fluid from the entire water column. In the case of the realizable $k-\varepsilon$ model, we can see the same characteristic secondary vortices around the inlet, and the boundary layer at the tank bottom. Two large secondary vortices can be seen at roughly R/3 and R2/3, indicating more intense mixing.

Figure 15. Turbulent kinetic energy (k) distribution.

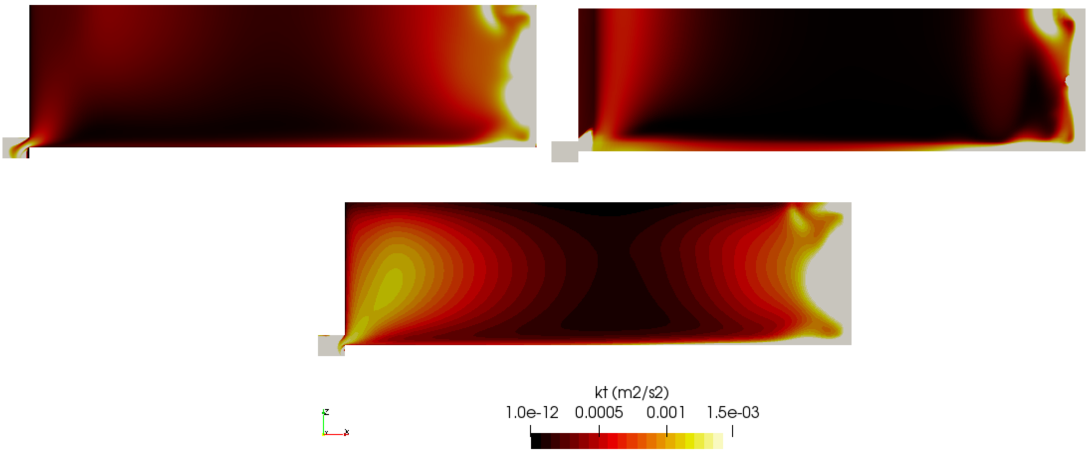

Note. k distribution for the following models: SST $k-\omega$ (top left), realizable $k-\varepsilon$ (top right) and $k-kl-\omega$ (bottom).

Figure 16. Eddy viscosity (ν_T) distribution.

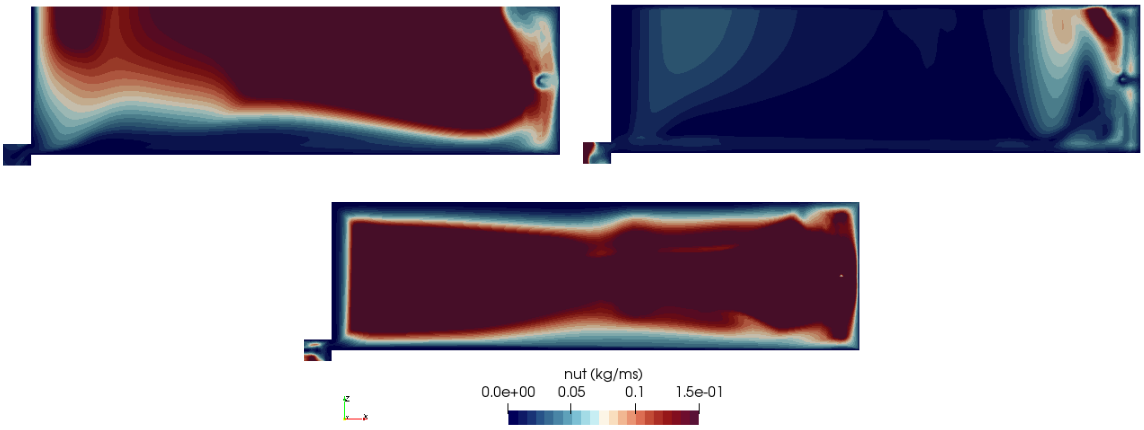

Note. ν_T distribution for the following models: SST $k-\omega$ (top left), realizable $k-\varepsilon$ (top right) and $k-kl-\omega$ (bottom).

Figure 17. Secondary flow structures.

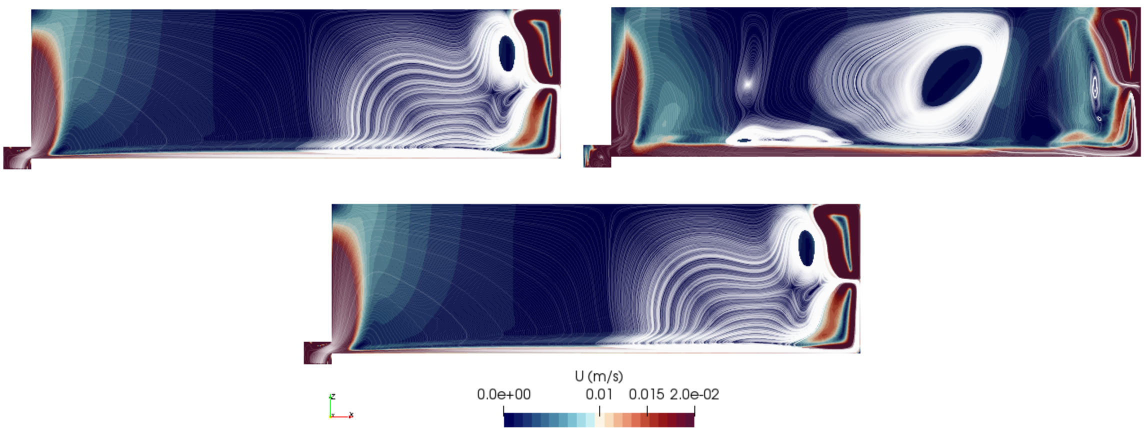

Note. Secondary velocity contours (axial and radial components) and streamlines depicting the secondary flow generated by the three models studied: SST $k-\omega$ (top left), realizable $k-\varepsilon$ (top right) and $k-kl-\omega$ (bottom).

As closing remarks, the correct implementation of the realizable $k - \varepsilon$ model is strongly dependent on the appropriate use of wall functions and on the cell discretization at the walls. It is a high-Re turbulence model with no damping functions so the first cell must lie in the range 30<y^+<200. It is advisable to stay as close as possible to y^+ values of 30 to make sure the first cell does not lie outside the logarithmic zone. No information regarding the velocities inside the boundary layer is available with this modelling approach. The calibration work gave a clear insight into the impact the boundary layer has on the resulting flow.

Small geometries with low characteristic velocities are challenging to model with this approach, as the boundary layer thickness can be very relevant. In larger geometries computation times are reduced as there is no need to discretize the boundary layer.

4.1.2. Inlet turbulence intensity

The next step consisted in the evaluation the inlet turbulent intensity. The following values of inlet turbulence intensities, I, were evluated: 5%, 10%, 20% and 50%. These values were computed in equation (24). Figure 18 shows the V_θ and β profiles at mid-height, Figure 19 shows the k contours, Figure 20 shows the ν_T contours and Figure 21 shows snapshots of the secondary flow structures generated in each case.

In relation to the tangential velocities, the results obtained with I up to 20% approximate very well the experimental result, with the best-fitting results obtained with $I = 20\%$. At $I = 50\%$ the bathtub vortex disappears.

As expected, the values of k and ν_T increase with I. Let us remember that for the $k - \varepsilon$ model the following relation holds:

$$\nu_T = C_\mu \frac{k^2}{\varepsilon} \tag{27}$$

In the realizable $k - \varepsilon$ model, the eddy viscosity does not increase with the square of the turbulent kinetic energy, as C_μ is not a constant but a function (Shih et al., 1995).

Figure 18. Effect of the inlet turbulent intensity on V_θ and β.

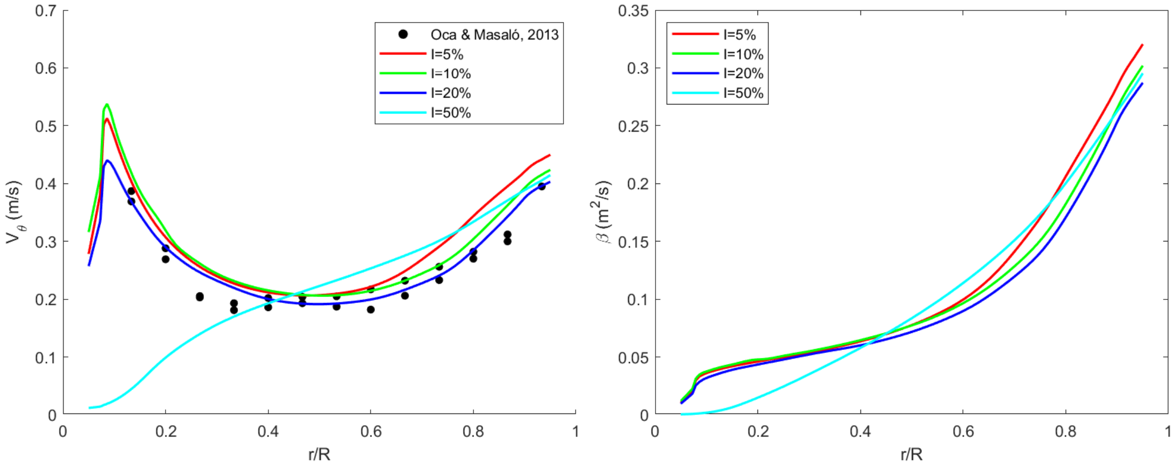

Note. A 50% inlet turbulent intensity eliminates the bathtub vortex in the outlet. Note that all the simulations were done with the same mesh.

Regarding the secondary flow structures, we can see the two vortices previously identified – generated by the inlet and the side wall – in all cases. The boundary layer along the tank floor, for values of I of up to 20%, appears to have a constant thickness. For the same values of I we can see three to four secondary vortices that expand throughout the entire water column up to a radial position of roughly R/3. From this point on, the bathtub vortex appears to collect fluid throughout the entire water column which is then conveyed toward the outlet.

Figure 19. k contours with different values of I.

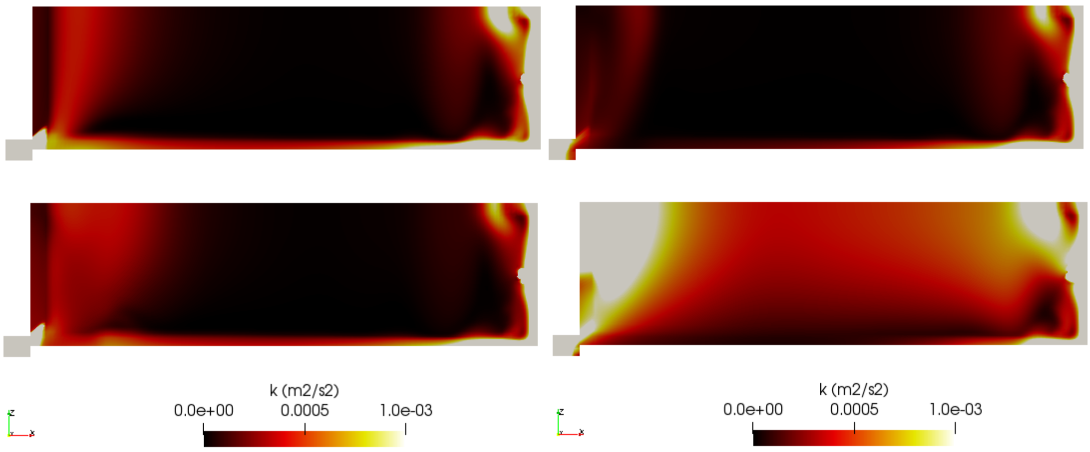

Note. k contours for the following inlet turbulence intensities (from left to right and from top to bottom): 5%, 10%, 20% and 50%.

Figure 20. ν_T contours with different values of I.

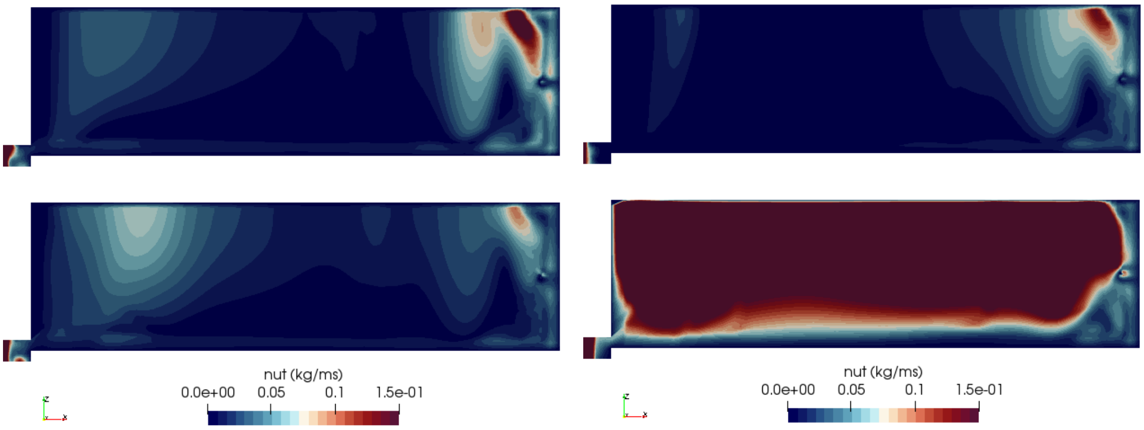

Note. ν_T contours for the following inlet turbulence intensities (from left to right and from top to bottom): 5%, 10%, 20% and 50%.

With $I =$ 50%, where the bathtub vortex is effectively dissipated, the secondary flow structure is practically deprived of secondary vortices, with the exception of the region close to the side walls and the inlet area. The forced vortex, though, is not dampened as expected. A possible explanation is that the same mesh was used in all cases, which present different resulting flows. This, in turn, means that the effective thickness of the boundary layer changes, and it is possible that some cells in the boundary layers are misplaced.

The results show that increasing the turbulent intensity at the inlet can result in the dissipation of the bathtub vortex in small tanks. Higher turbulence levels result in more intense mixing and the thickening of the boundary layer.

Figure 21. Secondary flow structures with different inlet turbulence intensities.

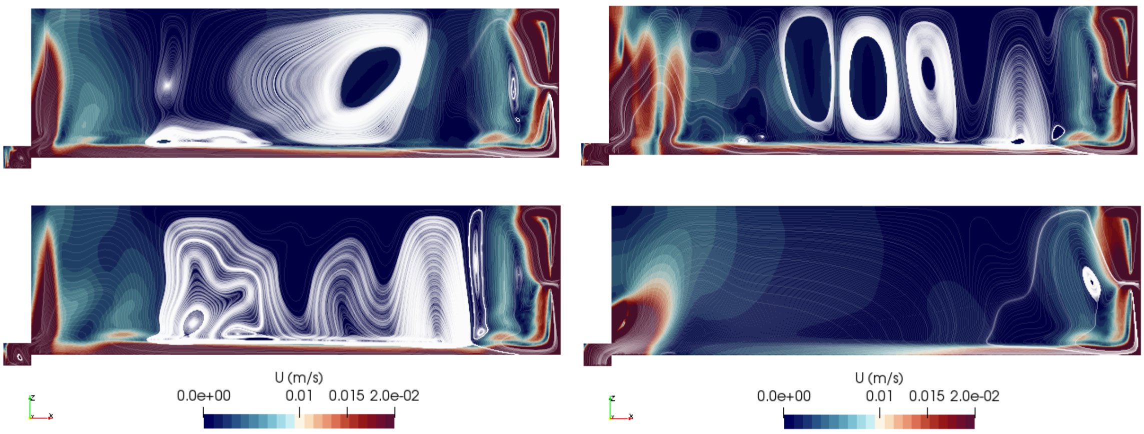

Note. Secondary velocity profiles (axial and radial components) and streamlines depicting the secondary flow generated with following inlet turbulence intensities (from left to right and top to bottom): 5%, 10%, 20% and 50%.

4.1.3. Torque balance and C_t

Table 8 shows the results obtained for the resistance torque equilibrium. The values of the resistance torque at the lateral walls, $T_{r,w}$, is the most important contribution in the system. This value was never higher than T_i. Nevertheless, the results show large discrepancies between the inlet torque, T_i, and the resistance torques, T_r. The negative difference indicates a resistance torque higher than the input torque.

Possible causes for these discrepancies may be related to the wall treatment in the realizable $k-\varepsilon$ model, where the value of τ_w (equation (18)) depends on the position of the first cell. The results may indicate the misplacement of cells in the boundary layer or underestimated τ_w values as the velocity gradient in the logarithmic zone is less accentuated than in the viscous sublayer of the buffer layer. The results show that in the SST $k-\omega$ model, where the boundary layer was discretized all the way down to the viscous sublayer, the lowest discrepancies were found. The bad results obtained with the $k-kl-\omega$ model may indicate an erroneous implementation of the initial conditions.

Another possible source of error is the dynamic nature of the system. The torque balance was done on a single timestep, and not on an average of various points in time. In the presence of a bathtub vortex, residuals rarely converged, but showed an oscillatory behaviour, indicating that the system did not reach equilibrium. The tangential component of the velocity had lower residuals than the axial and radial components, as is shown in Figure 22. In simulations were the bathtub vortex was damped, the residuals converged smoothly.

Table 8. Torque balance in each case

	Variables				
Turbulence model	I (%)	T_i/ρ	$T_{r,w}/\rho$	$T_{r,f}/\rho$	Diff.
SST $k-\omega$	5	6.0498e-06	4,279e-06	1,9947e-06	-3,70%
$k-kl-\omega$	5	6.0498e-06	5,244e-06	2,859e-06	-33,94%
realizable $k-\varepsilon$	5	6.0498e-06	5,288e-06	2,287e-06	-25,21%
realizable $k-\varepsilon$	10	6.0498e-06	4,201e-06	1,799e-08	30,26%
realizable $k-\varepsilon$	20	6.0498e-06	3,873e-06	1,711e-06	7,70%
realizable $k-\varepsilon$	50	6.0498e-06	3,684e-06	1,517e-06	14,03%

Note. Of the cases studied, the most accurate torque balance results were obtained with the SST $k-\omega$ model and the realizable $k-\varepsilon$ model with I=20%.

Table 9 shows the tank resistance coefficients, C_t, calculated using equation (20). The highest values of C_t were found in those cases with no bathtub vortex, which resulted in a reduction of V_1. The lowest value was found in the case with the $k-kl-\omega$ model, were all the velocities were overestimated.

Table 9. Average tangential velocities and resistance coefficients

Turbulence model	Variables		
	I (%)	V_1 (m/s)	C_t
SST $k-\omega$ and	5	0.219	0.0239
$k-kl-\omega$	5	0.312	0.0118
realizable $k-\varepsilon$	5	0.296	0.0128
realizable $k-\varepsilon$	10	0.290	0.0134
realizable $k-\varepsilon$	20	0.267	0.0159
realizable $k-\varepsilon$	50	0.221	0.0234

Note. Resistance coefficient, C_t, as a function of turbulence model, inlet turbulent intensity and resultant average tangential velocity.

Figure 22. Residuals in simulations with the realizable $k-\varepsilon$ and SST $k-\omega$ and models, I=5%.

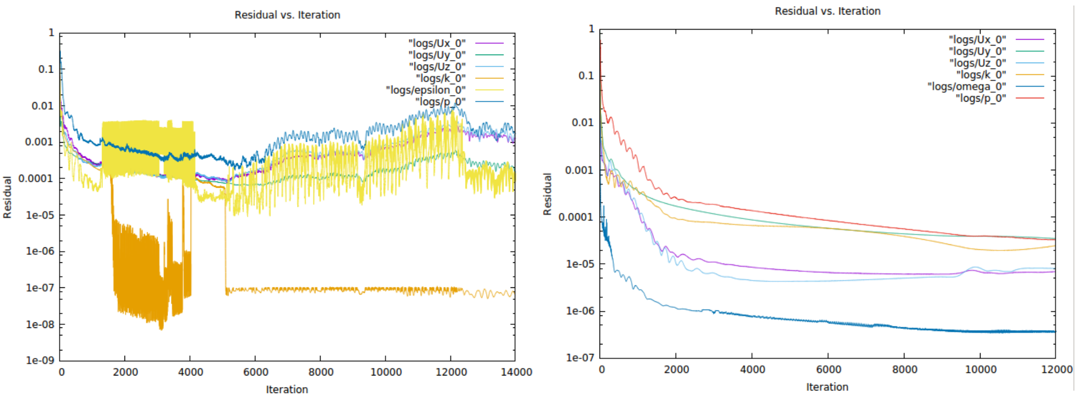

Note. When using the realizable $k-\varepsilon$ model (left), the tangential velocity residuals stabilize (with oscillations) at values of around 1e-04, whereas the other velocity components stabilize at higher residual values. The ε residuals show the greatest oscillations, indicating the dynamic nature of the system. In the SST $k-\omega$ model case (right) such oscillations were not present.

4.1.4. Reynolds number

Table 10 shows the effective Reynlods numbers calculated with the mean V_θ values for each case.

Table 10. Reynolds numbers in function of R, H and V_1, validation phase

Turbulence model	Variables		
	I (%)	Re_{R,V_1}	Re_{H,V_1}
SST $k-\omega$ and	5	161475	43060
$k-kl-\omega$	5	229725	61260
realizable $k-\varepsilon$	5	220650	58840

Note. Similar values were found in the $k-kl-\omega$ and realizable $k-\varepsilon$ models.

The results indicate that the characteristic value of Re for the validation case, using the tank radius R and the mean velocity V_1 as reference values, is ~2x10^5.

4.2. Production-size cases

4.2.1. Cases P1 to P4

Figure 23 shows the V_θ/V_{in} and β profiles for cases P1 to P4. The results show a transition, as size increases, from a bathtub vortex-dominated flow to a forced vortex-dominated flow. These results suggest that the scale has a big influence on the resulting hydrodynamics. β show almost horizontal profiles for cases P1 and P2, where the flow is dominated by the bathtub vortex, whereas the profiles in cases P2 and P3 indicate a forced vortex-dominated flow. Regarding the V_θ profiles, it is worth noting that in case P3 (D=20 m), the maximum value is found at a position of r/R=0.4. This indicates that the system was probably not in equilibrium.

Figure 23. V_θ and β profiles at H/2, cases P1 to P4

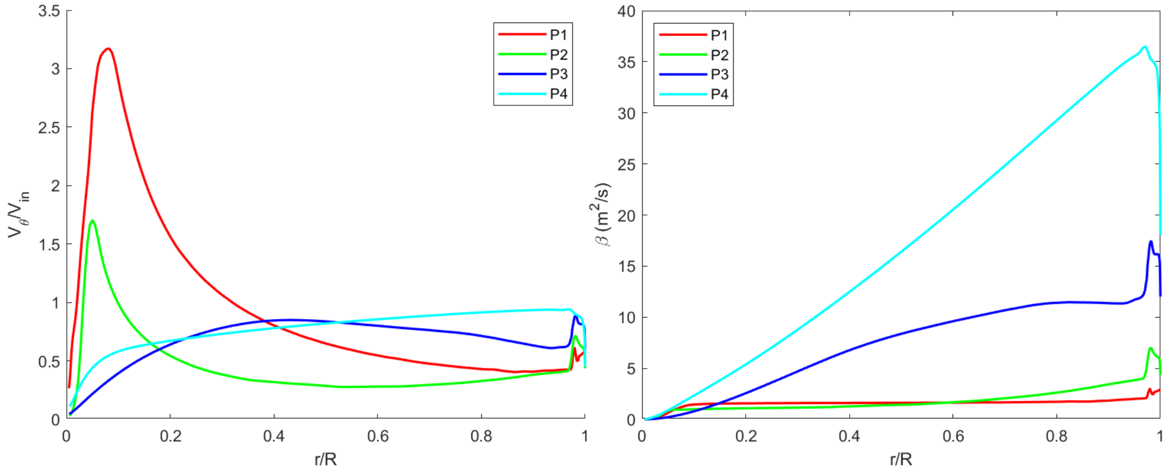

Note. The flow regime is strongly affected by the scale of the tank. In smaller geometries the bathtub vortex prevails and disappears as size increases.

Figure 24. V_θ profiles near the outlet at H/2 and close to the bottom, cases P3 and P4.

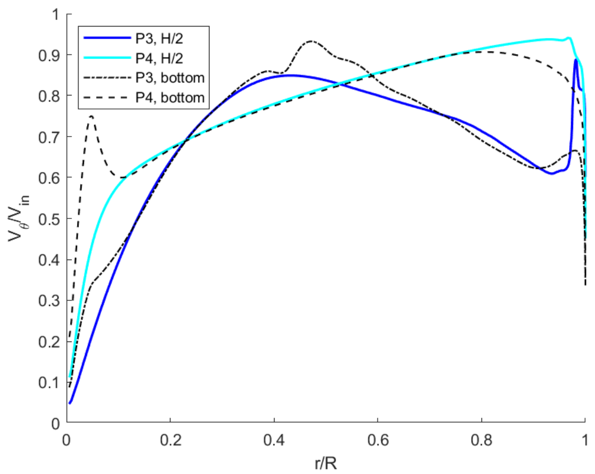

Note. In cases P3 and P4, a strongly dampened bathtub vortex can be observed at the outlet.

Figure 24 shows the V_θ profiles in cases P3 and P4 at H/2 and close to the bottom. As the figure shows, dampened bathtub vortices are found near the outlet.

Figure 25 shows the V_r profiles in cases P1 to P4 throughout the water column at R/2. The results show the existence of secondary vortices in case P1, whereas the profiles for cases P2 to P4 are relatively homogeneous. The highest velocities are found near the bottom, and the highest values were found in case P4. The results show the radial flow towards the outlet through the boundary layer.

Figure 26 shows the k contours for cases P1 to P4. The maximum values of k increased threefold between cases P1 and P2, from 0.012 m^2/s^2 to 0.036 m^2/s^2. In case P3 the maximum value reached 0.34 m^2/s^2 and in case P4 0.47 m^2/s^2. The highest values in all cases concentrate around the outlet and in cases P3 and P4 extend to the entire water column and into the rest of the tank.

Figure 25. V_r profiles throughout the water column at R/2, cases P1 to P4.

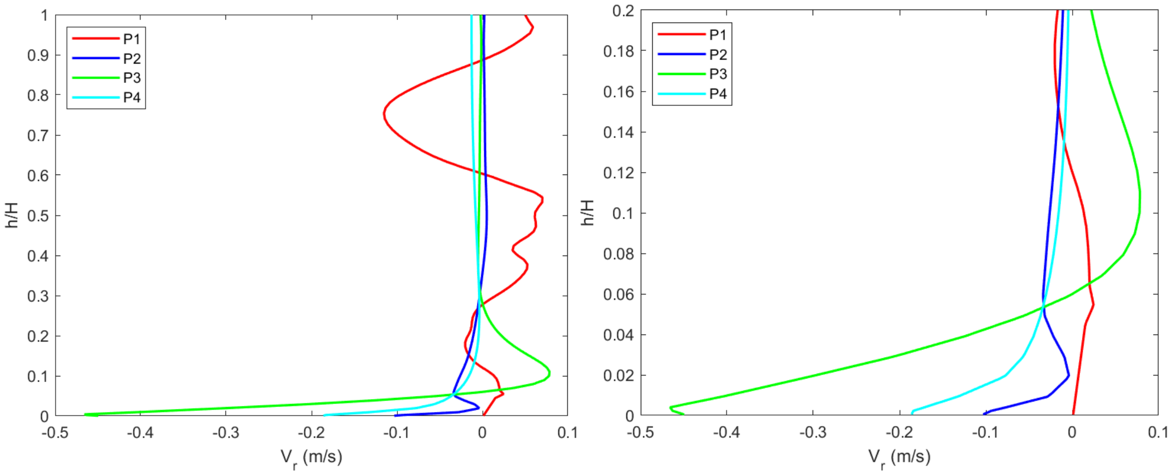

Note. The highest V_r values are found near the bottom surface at the boundary layer.

Figure 27 shows the ν_T contours for cases P1 to P4. The maximum values of ν_T increased from 0.25 kg/ms to 2.5 kg/ms between cases P1, P2. In cases P3 and P4 the maximum values were of around 200 kg/ms. The extent of the area occupied by higher ν_T values in case P3 is limited to the area around the central axis, whereas in case P4 it extends throughout most of the domain. These distributions are similar to the ones shown in Figure 20 for the SST $k-\omega$ and $k-kl-\omega$ turbulence models. These results indicate that higher turbulence levels are verified in bigger geometries, resulting in the containment of the bathtub vortex.

Figure 26. k contours, cases P1 to P4.

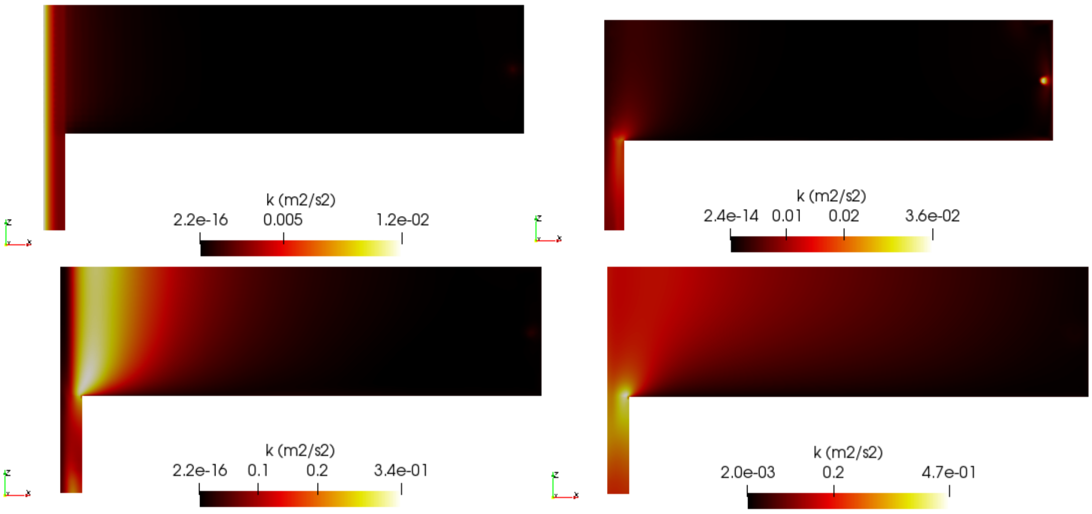

Note. k for cases P1 to P4 (from left to right and top to bottom). The maximum k values increased by a factor of three between cases P1 and P2 and by a factor of ten between cases P2 and P3.

Figure 28 shows snapshots of the secondary flow structures generated in each case. Case P1 presents more secondary structures and higher velocity gradients, which coincides with the highest values of V_θ around the axis. On the other side of the spectrum, case P4 presents a single vortex between the inlet, the tank side wall and the tank floor. The secondary flow towards the outlet passes mainly through the bottom boundary layer, a pattern which is not clear in the other cases.

Figure 27. ν_T contours, cases P1 to P4.

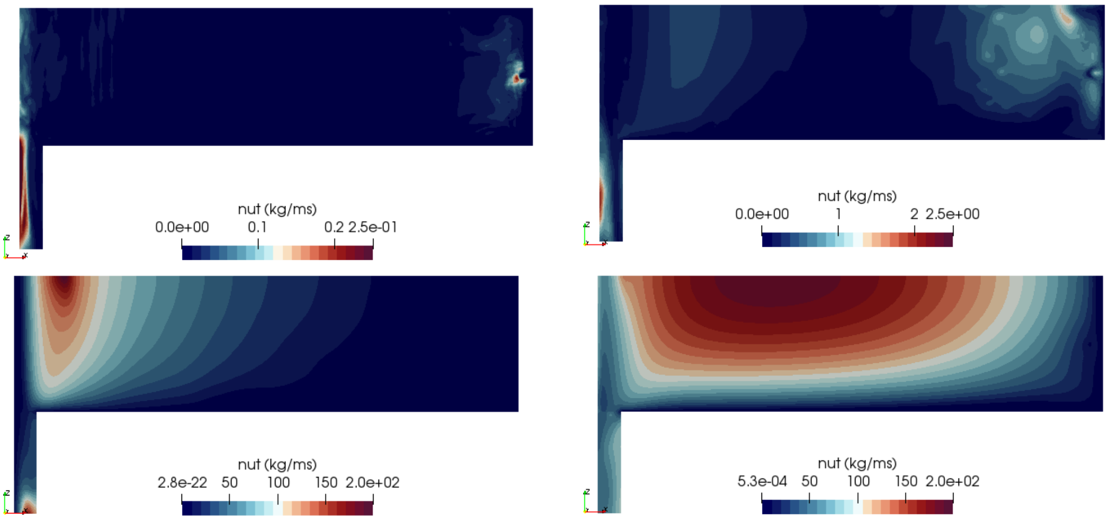

Note. ν_T for cases P1 to P4 (from left to right and top to bottom). The maximum ν_T values increased tenfold between cases P1 and P2 and hundredfold between cases P2 and P3.

Even though there appear to be less secondary vortices and mixing in cases P3 and P4, the k and ν_T distributions indicate the opposite. Higher values of k indicate more fluctuations in the mean velocity values. The RANS model, per definition, averages out these fluctuations, which cannot be visualized when looking at secondary flow velocity contours or streamlines.

Figure 28. Secondary flow structures, cases P1 to P4.

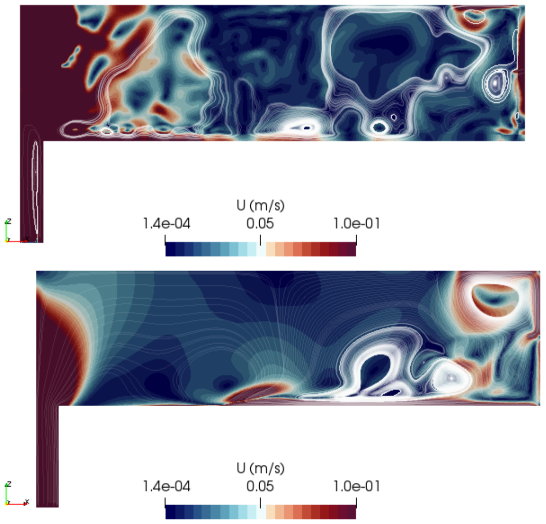

Note. Secondary velocity profiles (axial and radial components) and streamlines depicting the secondary flow generated in cases P1 to P4 (from left to right and top to bottom).

4.2.2. Cases P5.1, P5.2 and P5.3

Figure 29 shows the V_θ and β profiles for cases P5.1 to P5.3 at $H/2$. Figure 30 shows the V_θ profiles and in the vicinity of the outlet. The results are like those of cases P3 and P4, with the flow dominated by the forced vortex and the existence of a bathtub vortex at the outlet which is dampened in the rest of the domain. It is interesting to note that the maximum values of V_θ are higher than V_{in}, indicating that the system may not be in equilibrium.

Figure 29. V_θ and β profiles at H/2, cases P5.1 to P5.3.

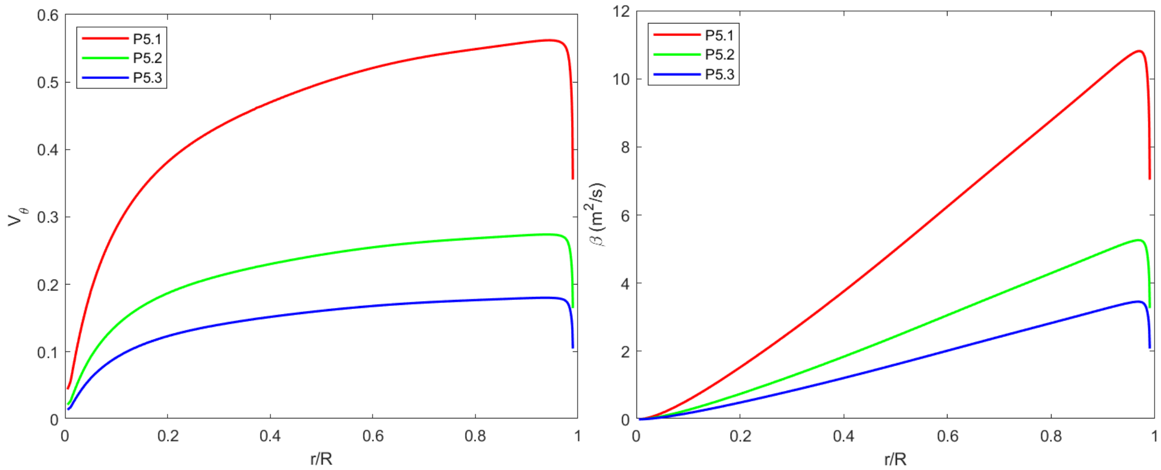

Note. The V_θ and β profiles in these cases suggest forced vortex-dominated flows.

Figure 30. V_θ profiles near the outlet at H/2 and close to the bottom, cases P5.1 to P5.3.

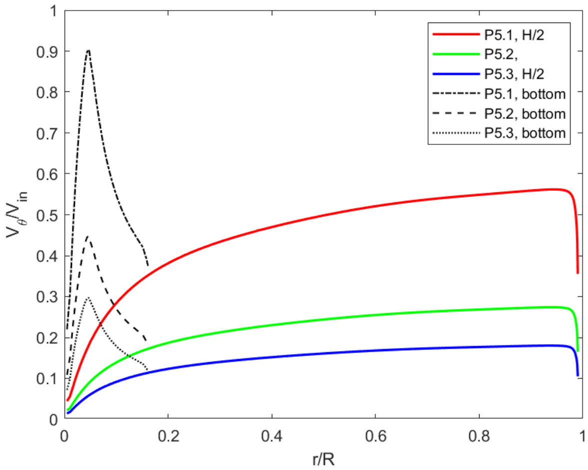

Note. Strong vortices are found at the bottom outlets.

Figure 31 shows the V_r profiles in cases P5.1 to P5.3 throughout the water column and near the bottom at R/2. The profiles are very constant and velocities increase close to the bottom wall. Higher values of Q result in higher velocities. There is a slight backflow just above the boundary layer.

Figure 32 shows the k contours for cases P5.1 to P5.3. The maximum values concentrate on the outlet region where the highest values of V_θ are found. The maximum values of k are a function of Q but their distribution is very similar in the three cases.

Figure 31. V_r profiles throughout the water column at R/2, cases P5.1 to P5.3.

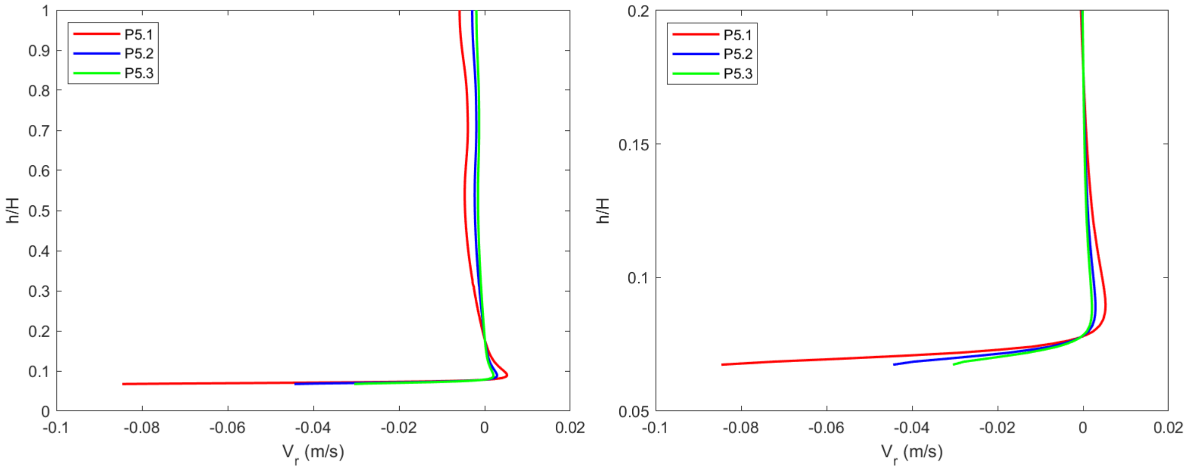

Note. The highest V_r values are found near the bottom surface at the boundary layer.

Figure 33 shows the ν_T contours for cases P5.1 to P5.3. The maximum values of ν_T in case P5.1 reach 80 kg/ms, whilst in case P5.2 they drop down to just below half, and in case P5.3 the maximum values are below 3 kg/ms. As in case P4, high ν_T values are present throughout most of the domain.

Figure 34 shows snapshots of the secondary flow structures in cases P5.1 to P5.3. The same structures can be observed in all three cases, with the strength of the flow being dictated by the value of Q. As in the validation cases and case P2, two secondary vortices form between the inlet and the side wall. Most of the transport towards the outlet seems to pass through the vicinity of the elliptical wall (bottom surface), with the presence of two weaker secondary vortices in the area adjacent to the outlet and the middle of the ellipse (this last vortex is difficult to see). The vertical flow in the tank axis collects fluid from the entire water column.

Figure 32. k contours, cases P5.1 to P5.3.

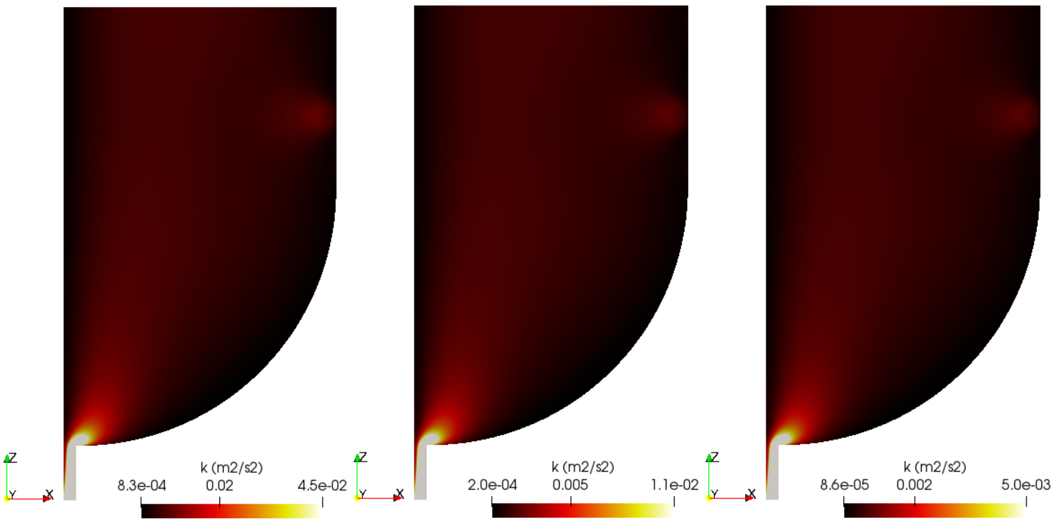

Note. Similar k distributions were found in cases P5.1 to P5.3 (from left to right).

Figure 33. ν_T contours, cases P5.1 to P5.3.

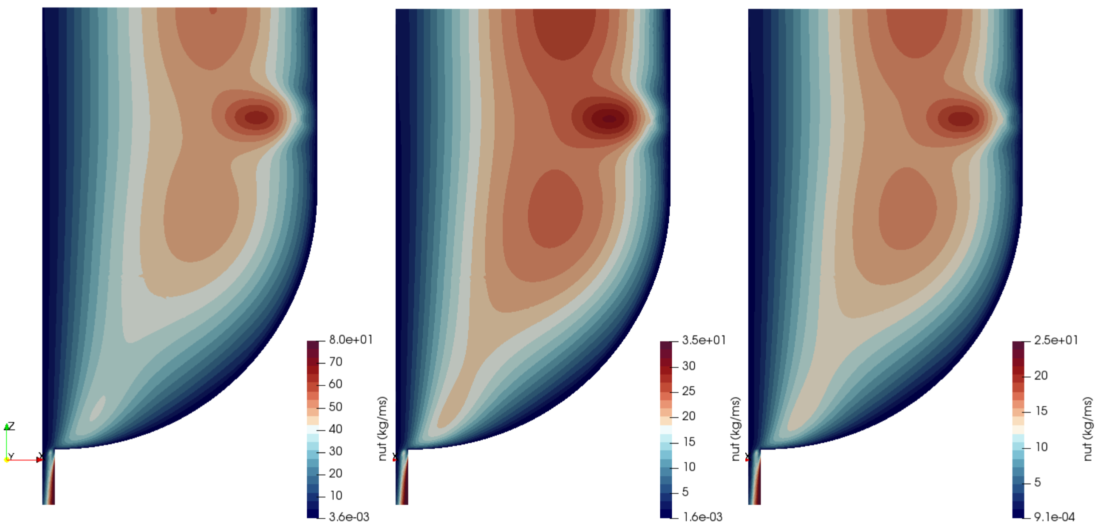

Note. Similar ν_T distributions were found in cases P5.1 to P5.3 (from left to right).

The k and ν_T distributions indicate intensive mixing throughout the domain, in particular in the bulk of the fluid. The two areas where these values are low are in the middle of the tank, throughout the water column, and in the vicinity of the walls. As the secondary flow velocity contours in Figure 34 show, in the centre of the tank there is a strong vertical flow towards the outlet. There is also flow through the boundary layer in the elliptic surface, but the area adjacent to it is characterized by low velocities and low turbulence intensities, indicating a zone with limited mixing.

Figure 34. Secondary flow structures, cases P5.1 to P5.3.

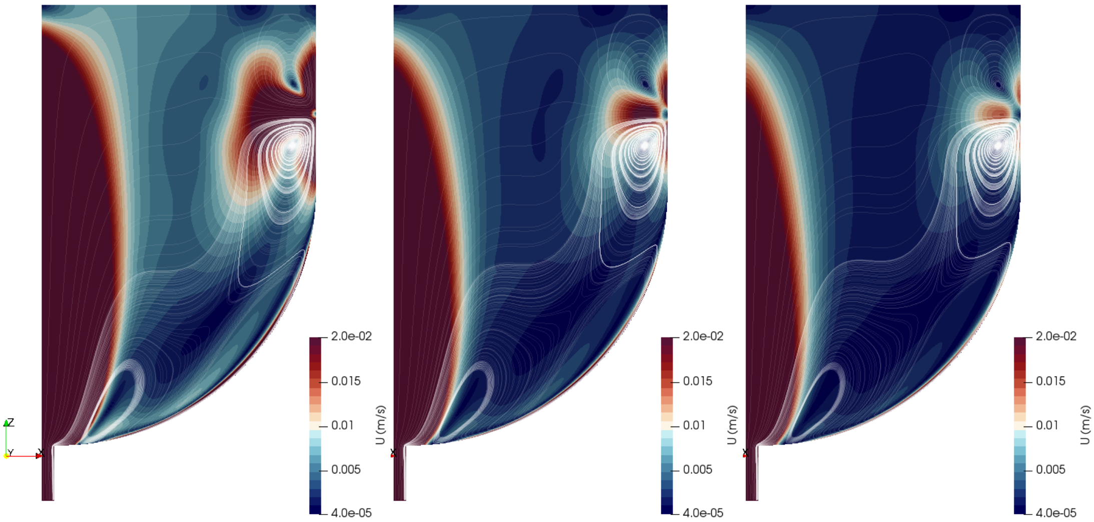

Note. Very similar flow structures are present in cases P5.1 to P5.3 (from left to right).

The results suggest that scaling has a strong impact on tank hydrodynamics. Bigger tank dimensions resulted in a substantial increase of turbulence levels, with higher k and ν_T values. For tanks with diameters above 10 m, the bathtub vortex is contained in the vicinity of the outlet and dissipated throughout the entire water column. This tells us that the flow structures in tanks of small dimensions differ strongly from the flow structures in larger tanks.

In smaller tanks, both bathtub vortex- and forced vortex-dominated flows can exist, depending on the volumetric flow rate. In bathtub vortex-dominated flows there is stronger mixing evidenced by the presence of multiple secondary vortices.

In tanks with diameters above 10 m, the results suggest that there are only forced vortex-dominated flows, regardless of the volumetric flow rate. The bathtub vortex is still present but contained in the vicinity of the outlet. Intensive mixing is evidenced by higher k values.

4.2.3. Torque balance and C_t

Table 11 shows the torque balance and Table 12 the C_t values for the prototype cases. Once again, the results show large discrepancies between the inlet torque, T_i, and the resistance torques, T_r. In this case, though, in most of the cases the resistance torque is underestimated. The possible reasons leading to these results have already been presented in chapter 4.1.3. In cases P1 and P2, $T_{r,w}$ dominates, whereas in cases P3 and P4, $T_{r,f}$ accounts for the most important contribution. In cases P5.1, P5.2 and P5.3, the elliptical surface is the bottom surface. In this case, the values of $T_{r,w}$ and $T_{r,f}$ are of the same order of magnitude.

Table 11. Torque balance, cases P1-P5

Turbulence model	Variables				
	$Vol.$ (m^3)	T_i/ρ	$T_{r,w}/\rho$	$T_{r,f}/\rho$	Diff.
P1	13	1.467e-03	1.974e-04	1.351e-04	77,3%
P2	105	2.326e-02	1.260e-02	7.739e-03	12,6%
P3	837	3.756e-01	1.555e-01	2.308e-01	-2,9%
P4	6698	5.989e+00	1.752e+00	2.522e+00	28,6%
P5.1	32751	2.227e+00	5.285e-01	5.995e-01	49,3%
P5.2	32751	5.848e-01	1.373e-01	1.584e-01	49,4%
P5.3	32751	2.396e-01	6.263e-02	7.283e-02	43,5%

Note. Of the cases studied, the most accurate torque balance results were obtained with the SST $k-\omega$ model and the realizable $k-\varepsilon$ model with I=20%.

The C_t values increase with the tank dimensions. In cases P5.1 to P5.3 the values seem to be constant. It would have been interesting to do simulations with the same value of Q but different V_{in} values.

Table 12. Average tangential velocities and resistance coefficients, cases P1-P5

Case	Variables		
	$Vol.$ (m^3)	V_1 (m/s)	C_t
P1	13	2.046	0.0003
P2	105	0.903	0.0034
P3	837	1.371	0.0034
P4	6698	1.524	0.0058
P5.1	32751	0.451	0.0081
P5.2	32751	0.221	0.0086
P5.3	32751	0.145	0.0085

Note. Resistance coefficient, C_t, as a function of volume, and resultant average tangential velocity.

4.2.4. Reynolds number

Table 13 and Figure 35 show the Reynolds numbers calculated in cases P1 to P5, where the main dimension is either the tank radius R or the tank depth H, and the reference velocity is the inlet velocity V_{in} or the mean tangential velocity V_1.

Table 13. Reynolds numbers in function of R, H, V_{in} and V_1, cases P5.1 to P5.3

Case	Variables			
	$Re_{R,V_{in}}$	$Re_{H,V_{in}}$	Re_{R,V_1}	Re_{H,V_1}
P1	5,05E+06	1,35E+06	5,12E+06	1,36E+06
P2	1,00E+07	2,67E+06	4,51E+06	1,20E+06
P3	2,02E+07	5,38E+06	1,37E+07	3,65E+06
P4	4,02E+07	1,07E+07	3,05E+07	8,12E+06
P5.1	1,00E+07	1,61E+07	9,01E+06	1,44E+07
P5.2	5,14E+06	8,23E+06	4,41E+06	7,06E+06
P5.3	3,29E+06	5,27E+06	2,91E+06	4,65E+06

Note. The values for Re change considerably with respect to the reference dimension and velocity values.

If we consider the biggest dimension as the reference length and V_1 as the reference velocity, we can conclude that the transition point where the bathtub vortex is dissipated by high turbulence levels lies roughly between $5x10^6$ and and $8x10^6$.

Figure 35. Reynolds numbers in function of R, H, V_{in} and V_1, cases P5.1 to P5.3.

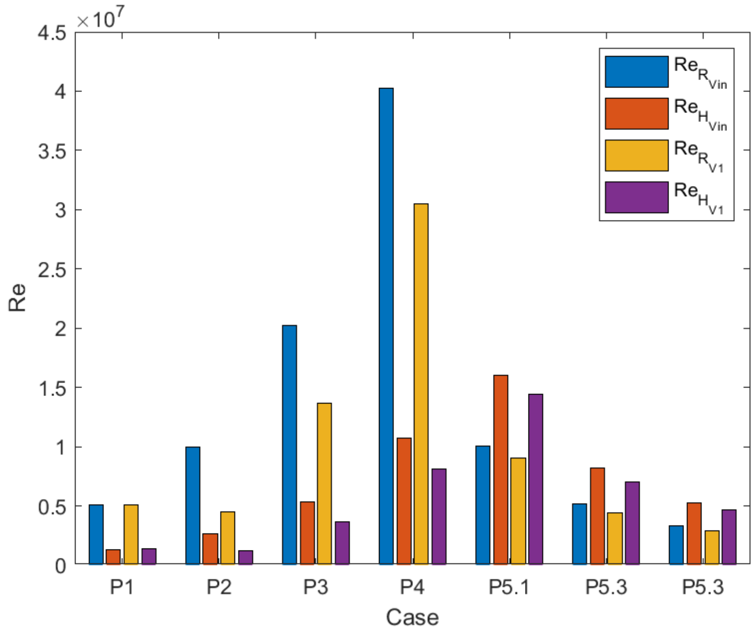

Note. The Re values calculated based on V_{in} are slightly overestimated.

5. Conclusions and future work

5.1. Conclusions

The specific objectives of this work were presented in chapter 3.1. Based on the validation and simulation work carried out, we can conclude the following:

1. **OpenFOAM model implementation and validation.**

The results show that an OpenFOAM model implementation – with the use of the realizable $k-\varepsilon$ model and cyclic boundary conditions – is capable of modelling the tangential velocity profile in small aquaculture tanks with tangential inlets and a single outlet in the bottom centre, in which a bathtub vortex and a forced vortex are clearly identifiable.

2. **Turbulence model performance.**

As already mentioned, only the realizable $k-\varepsilon$ model could model the bathtub vortex. When implementing the SST $k-\omega$ and $k-kl-\omega$ models, the eddy viscosity ν_T was overestimated, indicating higher turbulence levels. This resulted in the dissipation of the bathtub vortex throughout the water column.

3. **Impact of the inlet turbulence intensity on the resultant flow.**

Inlet turbulence intensity values of 50% effectively dissipated the bathtub vortex. This effect is similar to the one produced by relevant stocking densities of fish. Although this approach is an abstraction that does not take into consideration the effective distribution of turbulent kinetic energy inside the tank due to fish stocking densities and swimming behaviour, it may be a useful tool to evaluate operational condition ranges.

4. **Scaling effect on the tank hydrodynamics on geometries with diameters between 5 m and 40 m.**

The results suggest that scaling has a strong impact on tank hydrodynamics. The transition between bathtub vortex-dominated flows and forced vortex-dominated flows appears to happen at Re ~ 5x10^6 - 8x10^6, when the biggest tank dimension (H or R) and the mean velocity V_1 are considered. Above these Re values, the bathtub vortex is contained in the vicinity of the outlet and dissipated throughout the entire water column due to the increase in turbulence levels.

5.2. Future work

The entire operational range for salmon swimming velocities was not covered by the simulations. Further simulations on setups P1 to P5, with different values of V_{in} and HRT can be carried out.

The mapping of the scaling effect is incomplete. Geometries with intermediate values of D between 10 m and 20 m should be studied. The effect of the D/H ratio could be further studied with a new series of geometries with D/H rations ranging from 7.5 to 1.25.

Further validation work on experimental result on larger geometries is important. The evaluation of other turbulence models, such as RSM models, transient simulations, and the use of multiphase solvers to capture the free water surface are some possibilities for future work and research.

5. References

Almansa, C., Masaló, I., Reig, L., Piedrahita, R., & Oca, J. (2014). Influence of tank hydrodynamics on vertical oxygen stratification in flatfish tanks. *Aquacultural Engineering*, *63*, 1–8. https://doi.org/10.1016/j.aquaeng.2014.07.007

Andersen, A., Bohr, T., Stenum, B., Rasmussen, J. J., & Lautrup, B. (2006). The bathtub vortex in a rotating container. *Journal of Fluid Mechanics*, *556*, 121. https://doi.org/10.1017/S0022112006009463

Behroozi, L., & Couturier, M. F. (2019). Prediction of water velocities in circular aquaculture tanks using an axisymmetric CFD model. *Aquacultural Engineering*, *85*, 114–128. https://doi.org/10.1016/j.aquaeng.2019.03.005

Bergheim, A., Drengstig, A., Ulgenes, Y., & Fivelstad, S. (2009). Production of Atlantic salmon smolts in Europe—Current characteristics and future trends. *Aquacultural Engineering*, *41*(2), 46–52. https://doi.org/10.1016/j.aquaeng.2009.04.004

Burgers, J. M. (1948). A Mathematical Model Illustrating the Theory of Turbulence. In R. Von Mises & T. Von Kármán (Eds.), *Advances in Applied Mechanics* (Vol. 1, pp. 171–199). Elsevier. https://doi.org/10.1016/S0065-2156(08)70100-5

Burley, R., & Klapsis, A. (1985). Flow Distribution Studies in Fish Rearing Tanks. Part 2 Analysis of Hydraulic Performance of Im Square Tanks. *Aquacultural Engineering*, *4*, 22.

Burrows, R., & Chenowith, H. (1955). *Evaluation of three types of fish rearing ponds* (No. 39). US Department of the Interior, Fish and Wildlife Service. https://scholarworks.umass.edu/fishpassage_reports/459

Calabrese, S., Nilsen, T. O., Kolarevic, J., Ebbesson, L. O. E., Pedrosa, C., Fivelstad, S., Hosfeld, C., Stefansson, S. O., Terjesen, B. F., Takle, H., Martins, C. I. M., Sveier, H., Mathisen, F., Imsland, A. K., & Handeland, S. O. (2017). Stocking density limits for post-smolt Atlantic salmon (Salmo salar L.) with emphasis on production performance and welfare. *Aquaculture*, *468*, 363–370. https://doi.org/10.1016/j.aquaculture.2016.10.041

Chen, S., Timmons, M. B., Aneshansley, D. J., & Bisogni, J. J. (1993). Suspended solids characteristics from recirculating aquacultural systems and design implications. *Aquaculture*, *112*(2–3), 143–155. https://doi.org/10.1016/0044-8486(93)90440-A

Chu, Y. I., Wang, C. M., Park, J. C., & Lader, P. F. (2020). Review of cage and containment tank designs for offshore fish farming. *Aquaculture*, *519*, 734928. https://doi.org/10.1016/j.aquaculture.2020.734928

Chun, C., Vinci, B. J., & Timmons, M. B. (2018). Computational fluid dynamics characterization of a novel mixed cell raceway design. *Aquacultural Engineering*, *81*, 19–32. https://doi.org/10.1016/j.aquaeng.2018.02.002

Colbourne, D. B. (2005). Another perspective on challenges in open ocean aquaculture development. *IEEE Journal of Oceanic Engineering*, *30*(1), 4–11. https://doi.org/10.1109/JOE.2004.841399

Colt, J., & Watten, B. (1988). Applications of pure oxygen in fish culture. *Aquacultural Engineering*, *7*(6), 397–441. https://doi.org/10.1016/0144-8609(88)90003-9

Dalsgaard, J., Lund, I., Thorarinsdottir, R., Drengstig, A., Arvonen, K., & Pedersen, P. B. (2013). Farming different species in RAS in Nordic countries: Current status and future perspectives. *Aquacultural Engineering*, *53*, 2–13. https://doi.org/10.1016/j.aquaeng.2012.11.008

Davidson, J., & Summerfelt, S. (2004). Solids flushing, mixing, and water velocity profiles within large (10 and 150 m3) circular 'Cornell-type' dual-drain tanks. *Aquacultural Engineering*, *32*(1), 245–271. https://doi.org/10.1016/j.aquaeng.2004.03.009

Despres, B., & Couturier, M. (2006). Velocity profiles in mulit-drain circular tanks. In L. D. Hiemstra & Aquaculture Association of Canada (Eds.), *Aquaculture Canada 2006* (pp. 73–75). Aquaculture Association of Canada.

Duarte, S., Reig, L., Masaló, I., Blanco, M., & Oca, J. (2011). Influence of tank geometry and flow pattern in fish distribution. *Aquacultural Engineering*, *44*(2), 48–54. https://doi.org/10.1016/j.aquaeng.2010.12.002

Ecomerden AS. (2020). *Ecomwerden webpage*. https://www.ecomerden.com/

FishGLOBE AS. (2020). *FishGLOBE - lukket løsning for oppdrett av postsmolt*. https://www.fishglobe.no/

Fiskeridirektoratet. (2020). *Akvakultur*. Akvakultur. https://portal.fiskeridir.no/portal/apps/webappviewer/index.html?id=87d862c458774397a8466b148e3dd147

Føre, M., Alver, M. O., Alfredsen, J. A., Senneset, G., Espmark, Å., & Terjesen, B. F. (2018). Modelling how the physical scale of experimental tanks affects salmon growth performance. *Aquaculture*, *495*, 731–737. https://doi.org/10.1016/j.aquaculture.2018.06.057

Forsberg, O. I. (1995). Empirical investigations on growth of post-smolt Atlantic salmon (Salmo salar L.) in land-based farms. Evidence of a photoperiodic influence. *Aquaculture*, *133*(3), 235–248. https://doi.org/10.1016/0044-8486(95)00029-2

Geuzaine, C., & Remacle, J.-F. (2009). Gmsh: A three-dimensional finite element mesh generator with built-in pre-and post-processing facilities. *International Journal for Numerical Methods in Engineering*, 1309–1331.

Gorle, Jagan M.R., Terjesen, B. F., Holan, A. B., Berge, A., & Summerfelt, S. T. (2018). Qualifying the design of a floating closed-containment fish farm using computational fluid dynamics. *Biosystems Engineering*, *175*, 63–81. https://doi.org/10.1016/j.biosystemseng.2018.08.012

Gorle, J.M.R., Terjesen, B. F., Mota, V. C., & Summerfelt, S. (2018). Water velocity in commercial RAS culture tanks for Atlantic salmon smolt production. *Aquacultural Engineering*, *81*, 89–100. https://doi.org/10.1016/j.aquaeng.2018.03.001

Gorle, J.M.R., Terjesen, B. F., & Summerfelt, S. T. (2018). Hydrodynamics of octagonal culture tanks with Cornell-type dual-drain system. *Computers and Electronics in Agriculture*, *151*, 354–364. https://doi.org/10.1016/j.compag.2018.06.012

Gorle, J.M.R., Terjesen, B. F., & Summerfelt, S. T. (2019). Hydrodynamics of Atlantic salmon culture tank: Effect of inlet nozzle angle on the velocity field. *Computers and Electronics in Agriculture*, *158*, 79–91. https://doi.org/10.1016/j.compag.2019.01.046

Hauge Aqua AS. (2020). *Hauge Aqua*. Haugeaqua. https://haugeaqua.com/

Huguenin, J. E. (1997). The design, operations and economics of cage culture systems. *Aquacultural Engineering*, *16*(3), 167–203. https://doi.org/10.1016/S0144-8609(96)01018-7

Jeong, H. M., Chung, H. S., Kim, S. H., Choi, S. C., & Bae, K. Y. (2004). Fluid flow characteristics in the aquaculture tank for a breeding fish. *KSME International Journal*, *18*(12), 2265–2272. https://doi.org/10.1007/BF02990231

Kawakubo, T., Tsuchiya, Y., Sugaya, M., & Matsumura, K. (1978). Formation of a vortex around a sink: A kind of phase transition in a nonequilibrium open system. *Physics Letters A*, *68*(1), 65–66. https://doi.org/10.1016/0375-9601(78)90759-4

Key figures from Norwegian Aquaculture Industry 2018 (No. 1893–6946). (2019). Fiskeridirektoratet.

Klebert, P., Lader, P., Gansel, L., & Oppedal, F. (2013). Hydrodynamic interactions on net panel and aquaculture fish cages: A review. *Ocean Engineering*, *58*, 260–274. https://doi.org/10.1016/j.oceaneng.2012.11.006

Koskela, J., Pirhonen, J., & Jobling, M. (1997). Feed intake, growth rate and body composition of juvenile Baltic salmon exposed to different constant temperatures. *Aquaculture International*, *5*(4), 351–360. https://doi.org/10.1023/A:1018316224253

Lader, P., Fredriksson, D. W., Volent, Z., DeCew, J., Rosten, T., & Strand, I. M. (2017). Wave Response of Closed Flexible Bags. *Journal of Offshore Mechanics and Arctic Engineering*, *139*(5). https://doi.org/10.1115/1.4036676

Larmoyeux, J. D., Piper, R. G., & Chenoweth, H. H. (1973). Evaluation of Circular Tanks for Salmonid Production. *The Progressive Fish-Culturist*, *35*(3), 122–131. https://doi.org/10.1577/1548-8659(1973)35[122:EOCTFS]2.0.CO;2

Masaló, I., & Oca, J. (2016). Influence of fish swimming on the flow pattern of circular tanks. *Aquacultural Engineering*, *74*, 84–95. https://doi.org/10.1016/j.aquaeng.2016.07.001

McLean, E., Cotter, P., Thain, C., & King, N. (2008). TANK COLOR IMPACTS PERFORMANCE OF CULTURED FISH. *Croatian Journal of Fisheries : Ribarstvo*, *66*(2), 43–54.

Mota, V. C., Nilsen, T. O., Gerwins, J., Gallo, M., Ytteborg, E., Baeverfjord, G., Kolarevic, J., Summerfelt, S. T., & Terjesen, B. F. (2019). The effects of carbon dioxide on growth performance, welfare, and health of Atlantic salmon post-smolt (Salmo salar) in recirculating aquaculture systems. *Aquaculture*, *498*, 578–586. https://doi.org/10.1016/j.aquaculture.2018.08.075

Moukalled, F., Mangani, L., & Darwish, M. (2016). *The Finite Volume Method in Computational Fluid Dynamics*. Springer.

Nilsen, A., Hagen, Ø., Johnsen, C. A., Prytz, H., Zhou, B., Nielsen, K. V., & Bjørnevik, M. (2019). The importance of exercise: Increased water velocity improves growth of Atlantic salmon in closed cages. *Aquaculture*, *501*, 537–546. https://doi.org/10.1016/j.aquaculture.2018.09.057

Nilsen, A., Nielsen, K. V., Biering, E., & Bergheim, A. (2017). Effective protection against sea lice during the production of Atlantic salmon in floating enclosures. *Aquaculture*, *466*, 41–50. https://doi.org/10.1016/j.aquaculture.2016.09.009

Nordi, G. A., Glud, R. N., Gaard, E., & Simonsen, K. (2011). Environmental impacts of coastal fish farming; Carbon and Nitrogen budgets for trout farming in Kaldbacksfjord, Faroe Islands. *Marine Ecology - Progress Series*, *431*, 223–241.

Oca, J., & Masaló, I. (2007). Design criteria for rotating flow cells in rectangular aquaculture tanks. *Aquacultural Engineering*, *36*(1), 36–44. https://doi.org/10.1016/j.aquaeng.2006.06.001

Oca, J., & Masalo, I. (2013). Flow pattern in aquaculture circular tanks: Influence of flow rate, water depth, and water inlet & outlet features. *Aquacultural Engineering*, *52*, 65–72. https://doi.org/10.1016/j.aquaeng.2012.09.002

Odeh, M., Schrock, R. M., & Gannam, A. (2004). Comparative Hydraulics of Two Fishery Research Circular Tanks and Recommendations for Control of Experimental Bias. *Journal of Applied Aquaculture*, *14*(3–4), 1–23. https://doi.org/10.1300/J028v14n03_01

Papáček, Š., Petera, K., Masaló, I., & Oca, J. (2019). On the Optimization of Recirculated Aquaculture Systems. In H. C. Rodrigues, J. Herskovits, C. M. Mota Soares, A. L. Araújo, J. M. Guedes, J. O. Folgado, F. Moleiro, & J. F. A. Madeira (Eds.), *EngOpt 2018 Proceedings of the 6th International Conference on Engineering Optimization* (pp. 1229–1240). Springer International Publishing. https://doi.org/10.1007/978-3-319-97773-7_106

Plew, D. R., Klebert, P., Rosten, T. W., Aspaas, S., & Birkevold, J. (2015). Changes to flow and turbulence caused by different concentrations of fish in a circular tank. *Journal of Hydraulic Research*, *53*(3), 364–383. https://doi.org/10.1080/00221686.2015.1029016

Rankine, W. J. M., & Roberts, V. L. (1858). *A manual of applied mechanics*. R. Griffin.

Rasmussen, M. R., Laursen, J., Craig, S. R., & McLean, E. (2005). Do fish enhance tank mixing? *Aquaculture*, *250*(1–2), 162–174. https://doi.org/10.1016/j.aquaculture.2005.02.041

Rasmussen, M. R., & McLean, E. (2004). Comparison of two different methods for evaluating the hydrodynamic performance of an industrial-scale fish-rearing unit. *Aquaculture*, *242*(1–4), 397–416. https://doi.org/10.1016/j.aquaculture.2004.08.045

Remen, M., Solstorm, F., Bui, S., Klebert, P., Vågseth, T., Solstorm, D., Hvas, M., & Oppedal, F. (2016). Critical swimming speed in groups of Atlantic salmon Salmo salar. *Aquaculture Environment Interactions*, *8*, 659–664. https://doi.org/10.3354/aei00207

Scale AQ. (2020). *Flytekrager*. Aqualine. http://aqualine.no/produkter/flytekrager

Shainee, M., Leira, B. J., Ellingsen, H., & Fredheim, A. (2013). *An Optimum Design Concept for Offshore Cage Culture*. 85–93. https://doi.org/10.1115/OMAE2012-83601

Shih, T.-H., Liou, W. W., Shabbir, A., Yang, Z., & Zhu, J. (1995). A new k-ϵ eddy viscosity model for high reynolds number turbulent flows. *Computers & Fluids*, *24*(3), 227–238. https://doi.org/10.1016/0045-7930(94)00032-T

Solstorm, F., Solstorm, D., Oppedal, F., Fernö, A., Fraser, T., & Olsen, R. (2015). Fast water currents reduce production performance of post-smolt Atlantic salmon Salmo salar. *Aquaculture Environment Interactions*, *7*(2), 125–134. https://doi.org/10.3354/aei00143

Strand, I. M., Sørensen, A. J., Lader, P., & Volent, Z. (2013). Modelling of Drag Forces on a Closed Flexible Fish Cage. *IFAC Proceedings Volumes*, *46*(33), 340–345. https://doi.org/10.3182/20130918-4-JP-3022.00014

Summerfelt, S. T., Mathisen, F., Holan, A. B., & Terjesen, B. F. (2016). Survey of large circular and octagonal tanks operated at Norwegian commercial smolt and post-smolt sites. *Aquacultural Engineering*, *74*, 105–110. https://doi.org/10.1016/j.aquaeng.2016.07.004

Taranger, G. L., Karlsen, Ø., Bannister, R. J., Glover, K. A., Husa, V., Karlsbakk, E., Kvamme, B. O., Boxaspen, K. K., Bjørn, P. A., Finstad, B., Madhun, A. S., Morton, H. C., & Svåsand, T. (2015). Risk assessment of the environmental impact of Norwegian Atlantic salmon farming. *ICES Journal of Marine Science*, *72*(3), 997–1021. https://doi.org/10.1093/icesjms/fsu132

Terjesen, B. F., Summerfelt, S. T., Nerland, S., Ulgenes, Y., Fjæra, S. O., Megård Reiten, B. K., Selset, R., Kolarevic, J., Brunsvik, P., Bæverfjord, G., Takle, H., Kittelsen, A. H., & Åsgård, T. (2013). Design, dimensioning, and performance of a research facility for studies on the requirements of fish in RAS environments. *Aquacultural Engineering*, *54*, 49–63. https://doi.org/10.1016/j.aquaeng.2012.11.002

The State of World Fisheries and Aquaculture 2020. (2020). FAO. https://doi.org/10.4060/ca9229en

Thorarensen, H., & Farrell, A. P. (2011). The biological requirements for post-smolt Atlantic salmon in closed-containment systems. *Aquaculture*, *312*(1–4), 1–14. https://doi.org/10.1016/j.aquaculture.2010.11.043

Timmons, M. B., Summerfelt, S. T., & Vinci, B. J. (1998). Review of circular tank technology and management. *Aquacultural Engineering*, *18*(1), 51–69. https://doi.org/10.1016/S0144-8609(98)00023-5

Tvinnereim, K., & Skybakmoen, S. (1989). Water exchange and self-cleaning in fish-rearing tanks. *Aquaculture: A Biotechnology in Progress. European Aquaculture Society, Bredene, Belgium*, 7.

Verhoeven, J. T. P., Salvo, F., Knight, R., Hamoutene, D., & Dufour, S. C. (2018). Temporal Bacterial Surveillance of Salmon Aquaculture Sites Indicates a Long Lasting Benthic Impact With Minimal Recovery. *Frontiers in Microbiology*, *9*. https://doi.org/10.3389/fmicb.2018.03054

Weller, H. G., Tabor, G., Jasak, H., & Fureby, C. (1998). A tensorial approach to computational continuum mechanics using object-oriented techniques. *Computers in Physics*, *12*(6), 620–631. https://doi.org/10.1063/1.168744

Yukimoto, S., Niino, H., Noguchi, T., Kimura, R., & Moulin, F. Y. (2010). Structure of a bathtub vortex: Importance of the bottom boundary layer. *Theoretical and Computational Fluid Dynamics*, *24*(1–4), 323–327. https://doi.org/10.1007/s00162-009-0128-3

Appendix A

Gmsh script for case P5

```
// Gmsh project created on Thu May 28 16:17:55 2020
SetFactory("OpenCASCADE");
//+
Geometry.Tolerance = 1e-9;
a=0.665; //Case 4, 12deg sector, Q=2,2-6.7 m3/s
in=a;
//Mesh refinement
A=1;
B=1;//2, 1.5, 1, 0.75 y 0.5
C=A/B;
//
x0=0.1;
x1=19.6;
y1=16;
y2=y1/2;
//in=0.42275;
y3=y2+in/2;
y4=y2-in/2;
y5=-y1;
bl=0.05;
y6=y5+bl;
R=20;
R1=R-bl;
R2=x1-in;
R3=4;
R4=18.69;//19.28;
do=1;
do2=do-bl;
do3=0;
ho=5;
th2=1.5;
th3=10;
yo=-20;//ho+y5;
y_slope=y5+((R3-do)*(-y5-bl)/(R-do));
theta0=Asin(((0.9*do)-(R-R4))/(R4));//0;
theta1=0.6;//0.83
theta2=45;
theta3=Acos((do-(R-R4))/(R4));//84.3;
theta4=Asin((do-(R-R4))/(R4));
//+
Point(1) = {x0, 0, y5+R4-(R4-1*bl)*Cos(theta0*Pi/180), 1.0};
//+
Point(2) = {x0, 0, y1, 1,0};
//+
Point(3) = {R, 0, y1, 1,0};
//+
//Point(4) = {R, 0, 0, 1,0};
//+
Point(7) = {do+do3, 0, yo, 1,0};
//+
Point(8) = {x0, 0, yo, 1,0};
//+
//Point(11) = {R1, 0, bl, 1.0};
//+
Point(12) = {R1, 0, y1, 1.0};
//+
Point(13) = {R1, 0, y4, 1.0};
//+
Point(14) = {R2, 0, y4, 1.0};
//+
```

```
Point(15) = {R2, 0, y3, 1.0};
//+
Point(16) = {R1, 0, y3, 1.0};
//+
Point(17) = {(R-R4)+(R4-bl)*Sin(theta0)+do3/2, 0, yo, 1.0};
//+
Point(18) = {R, 0, y4, 1.0};
//+
Point(19) = {R, 0, y3, 1.0};
//+
Line(5) = {3, 19};
//+
Line(6) = {19, 18};
//+
//Point(21) = {R3, 0, y_slope, 1.0};
//+
//Point(22) = {R3-bl, 0, y_slope+bl, 1.0};
//+
Point(24) = {R-R4, 0, y5+R4, 1.0};
//+
Point(25) = {(R-R4)+(R4-bl)*Sin(theta0), 0, y5+R4-(R4-bl)*Cos(theta0), 1.0};
//+
Point(26)  =  {(R-R4)+(R4-bl)*Sin(theta2*Pi/180),  0,  y5+R4-(R4-bl)*Cos(theta2*Pi/180),
1.0};
//+
Point(27) = {(R-R4)+(R4-bl)*Sin(theta3), 0, y5+R4-(R4-bl)*Cos(theta3), 1.0};
//+
Point(28) = {(R-R4)+(R4)*Sin(theta4), 0, y5+R4-(R4)*Cos(theta4), 1.0};
//+
Point(29) = {(R-R4)+(R4)*Sin(theta2*Pi/180), 0, y5+R4-(R4)*Cos(theta2*Pi/180), 1.0};
//+
Point(30) = {(R-R4)+(R4)*Sin(theta3), 0, y5+R4-(R4)*Cos(theta3), 1.0};
//+
Point(31) = {R-th2, 0, y1, 1.0};
//+
Point(32) = {(R-R4)+(R4)*Sin(theta0), 0, y1, 1.0};
//+
Point(33) = {(R-R4)+(R4-bl)*Sin(theta4), 0, y5+R4-(R4-bl)*Cos(theta4), 1.0};
//+
Point(34) = {(R-R4)+(R4-bl)*Sin(theta0), 0, y5+R4-(R4)*Cos(theta0), 1.0};
//+
Point(35) = {x0, 0, y5+R4-(R4)*Cos(theta0), 1.0};
//+
Point(36) = {(R-R4)+(R4)*Sin(theta4), 0, y1, 1.0};
//+
Point(37) = {x1, 0, y4, 1.0};
//+
Point(38) = {x1, 0, y3, 1.0};
//+
Point(39) = {(R-R4)+(R4-th2)*Sin(theta2*Pi/180), 0, y5+R4-(R4-th2)*Cos(theta2*Pi/180),
1.0};
//+
Point(40) = {(R-R4)+(R4-th2)*Sin(theta3), 0, y5+R4-(R4-th2)*Cos(theta3), 1.0};
//+
Point(41) = {(R-R4)+(R4)*Sin(theta4), 0, y5+R4-(R4-bl)*Cos(theta3), 1.0};
//+
Point(42) = {(R-R4)+(R4)*Sin(theta0), 0, y5+R4-(R4-bl)*Cos(theta3), 1.0};
//+
Point(43) = {x0, 0, y5+R4-(R4-bl)*Cos(theta3), 1.0};
//+
```

```
Point(44) = {(R-R4)+(R4-th2)*Sin(theta4), 0, y5+R4-(R4-th2)*Cos(theta4), 1.0};
//+
Point(45) = {x0, 0, y5+R4-(R4-th2)*Cos(theta4), 1.0};
//+
Point(46) = {(R-R4)+(R4-bl)*Sin(theta0), 0, y5+R4-(R4-th2)*Cos(theta4), 1.0};
//+
Point(47) = {(R-R4)+(R4-th3)*Sin(theta2*Pi/180), 0, y5+R4-(R4-th3)*Cos(theta2*Pi/180),
1.0};
//+
Point(48) = {(R-R4)+(R4-th3)*Sin(theta2*Pi/180), 0,  y5+R4-(R4-th2)*Cos(theta3), 1.0};
//+
Point(49) = {(R-R4)+(R4-th3)*Sin(theta2*Pi/180), 0,  y1, 1.0};
//+
Point(50) = {(R-R4)+(R4)*Sin(theta4), 0, y5+R4-(R4-th3)*Cos(theta2*Pi/180), 1.0};
//+
Point(51) = {(R-R4)+(R4)*Sin(theta0), 0, y5+R4-(R4-th3)*Cos(theta2*Pi/180), 1.0};
//+
Point(52) = {x0, 0, y5+R4-(R4-th3)*Cos(theta2*Pi/180), 1.0};
//+
Circle(7) = {27, 24, 26};
//+
Circle(8) = {26, 24, 33};
//+
Circle(9) = {30, 24, 29};
//+
Circle(10) = {29, 24, 28};
//+
Line(11) = {18, 30};
//+
Line(12) = {12, 16};
//+
Line(13) = {16, 13};
//+
Line(14) = {15, 14};
//+
Line(15) = {13, 27};
//+
Line(17) = {28, 7};
//+
Line(18) = {8, 17};
//+
Line(19) = {17, 7};
//+
Line(20) = {1, 25};
//+
Line(22) = {26, 29};
//+
Line(23) = {27, 30};
//+
Line(24) = {13, 18};
//+
Line(25) = {16, 19};
//+
Line(26) = {15, 38};
//+
Line(27) = {14, 37};
//+
Line(28) = {12, 3};
//+
//Line(29) = {2, 1};
```

```
//+
//Line(30) = {32, 25};
//+
//Line(31) = {31, 26};
//+
Line(32) = {2, 32};
//+
Line(34) = {31, 12};
//+
Line(35) = {1, 35};
//+
Line(36) = {35, 8};
//+
Line(37) = {25, 34};
//+
Line(38) = {34, 17};
//+
Line(39) = {33, 28};
//+
Line(40) = {34, 28};
//+
Line(41) = {35, 34};
//+
Line(42) = {25, 33};
//+
Line(43) = {32, 36};
//+
Line(44) = {36, 49};
//+
//Line(45) = {36, 33};
//+
Line(46) = {38, 37};
//+
Circle(47) = {40, 24, 39};
//+
Circle(48) = {39, 24, 44};
//+
Line(49) = {40, 27};
//+
Line(50) = {39, 26};
//+
Line(51) = {44, 33};
//+
Line(52) = {31, 40};
//+
Line(53) = {45, 46};
//+
Line(54) = {46, 44};
//+
Line(55) = {43, 42};
//+
Line(56) = {42, 41};
//+
Line(57) = {41, 48};
//+
Line(58) = {2, 43};
//+
Line(59) = {43, 52};
//+
Line(60) = {45, 1};
```

```
//+
Line(61) = {32, 42};
//+
Line(62) = {42, 51};
//+
Line(63) = {46, 25};
//+
Line(64) = {36, 41};
//+
Line(65) = {41, 50};
//+
Line(66) = {52, 45};
//+
Line(67) = {51, 46};
//+
Line(68) = {50, 44};
//+
Line(69) = {49, 31};
//+
Line(70) = {48, 40};
//+
Line(71) = {49, 48};
//+
Line(72) = {48, 47};
//+
Line(73) = {47, 39};
//+
Line(74) = {50, 47};
//+
Line(75) = {52, 51};
//+
Line(76) = {51, 50};
//+
Curve Loop(1) = {18, -38, -41, 36};
//+
Plane Surface(1) = {1};
//+
Curve Loop(2) = {17, -19, -38, 40};
//+
Plane Surface(2) = {2};
//+
Curve Loop(3) = {40, -39, -42, 37};
//+
Plane Surface(3) = {3};
//+
Curve Loop(4) = {41, -37, -20, 35};
//+
Plane Surface(4) = {4};
//+
Curve Loop(5) = {20, -63, -53, 60};
//+
Plane Surface(5) = {5};
//+
Curve Loop(6) = {42, -51, -54, 63};
//+
Plane Surface(6) = {6};
//+
Curve Loop(7) = {53, -67, -75, 66};
//+
Plane Surface(7) = {7};
```

```
//+
Curve Loop(8) = {54, -68, -76, 67};
//+
Plane Surface(8) = {8};
//+
Curve Loop(9) = {10, -39, -8, 22};
//+
Plane Surface(9) = {9};
//+
Curve Loop(10) = {8, -51, -48, 50};
//+
Plane Surface(10) = {10};
//+
Curve Loop(11) = {48, -68, 74, 73};
//+
Plane Surface(11) = {11};
//+
Curve Loop(12) = {75, -62, -55, 59};
//+
Plane Surface(12) = {12};
//+
Curve Loop(13) = {76, -65, -56, 62};
//+
Plane Surface(13) = {13};
//+
Curve Loop(14) = {74, -72, -57, 65};
//+
Plane Surface(14) = {14};
//+
Curve Loop(15) = {55, -61, -32, 58};
//+
Plane Surface(15) = {15};
//+
Curve Loop(16) = {56, -64, -43, 61};
//+
Plane Surface(16) = {16};
//+
Curve Loop(17) = {57, -71, -44, 64};
//+
Plane Surface(17) = {17};
//+
Curve Loop(18) = {9, -22, -7, 23};
//+
Plane Surface(18) = {18};
//+
Curve Loop(19) = {7, -50, -47, 49};
//+
Plane Surface(19) = {19};
//+
Curve Loop(20) = {47, -73, -72, 70};
//+
Plane Surface(20) = {20};
//+
Curve Loop(21) = {70, -52, -69, 71};
//+
Plane Surface(21) = {21};
//+
Curve Loop(22) = {23, -11, -24, 15};
//+
Plane Surface(22) = {22};
```

```
//+
Curve Loop(23) = {24, -6, -25, 13};
//+
Plane Surface(23) = {23};
//+
Curve Loop(24) = {25, -5, -28, 12};
//+
Plane Surface(24) = {24};
//+
Curve Loop(25) = {27, -46, -26, 14};
//+
Plane Surface(25) = {25};
//+
Curve Loop(26) = {13, 15, -49, -52, 34, 12};
//+
Curve Loop(27) = {27, -46, -26, 14};
//+
Plane Surface(26) = {26, 27};
//+
//Discretización
nr1=12;
nr2=50*C;
nr2b=2.5*nr2;
nr3=50*C;
nv1=30*C;
nv2=20*C;
nv3=60*C;
nv4=80*C;
nv4a=(2/3)*nv4;
nv4b=(1/3)*nv4;
nin=4;
nbl=4;
//+
Transfinite Curve {18, 41, 20, 53, 75, 55, 32} = nr1 Using Progression 0.90;
//+
Transfinite Curve {10, 8, 48} = nr2b Using Progression 1;//0.97;
//+
Transfinite Curve {74, 57, 44} = nr2b Using Progression 1;//1.01;
//+
Transfinite Curve {9, 7, 47, 72, 65, 62, 59} = nr2 Using Progression 1;
//+
Transfinite Curve {36, 38, 17} = nv1 Using Progression 1;
//+
Transfinite Curve {60, 63, 51, 50, 49, 34} = nv2 Using Progression 0.95;
//+
Transfinite Curve {66, 67, 68, 73, 70, 69} = nv3 Using Progression 1;
//+
Transfinite Curve {58, 61, 64, 71, 52} = nv4 Using Progression 1;
//+
Transfinite Curve {5, 12} = nv4a Using Progression 1;
//+
Transfinite Curve {11, 15} = nv4b Using Progression 1;
//+
Transfinite Curve {14, 46, 26, 27, 13, 6} = nin Using Progression 1;
//+
Transfinite Curve {35, 37, 24, 25} = nbl Using Progression 0.8;
//+
Transfinite Curve {19, 40, 42, 54, 76, 56, 43} = 4 Using Progression 1;
//+
Transfinite Curve {39, 22} = nbl Using Progression 0.5;
```

```
//+
Transfinite Curve {23, 28} = nbl Using Progression 0.5;
//+
Transfinite Surface {1};
//+
Transfinite Surface {2};
//+
Transfinite Surface {4};
//+
Transfinite Surface {5};
//+
Transfinite Surface {3};
//+
Transfinite Surface {6};
//+
Transfinite Surface {7};
//+
Transfinite Surface {8};
//+
Transfinite Surface {12};
//+
Transfinite Surface {13};
//+
Transfinite Surface {15};
//+
Transfinite Surface {16};
//+
Transfinite Surface {17};
//+
Transfinite Surface {18};
//+
Transfinite Surface {21};
//+
Transfinite Surface {14};
//+
Transfinite Surface {20};
//+
Transfinite Surface {11};
//+
Transfinite Surface {10};
//+
Transfinite Surface {19};
//+
Transfinite Surface {9};
//+
Transfinite Surface {19};
//+
Transfinite Surface {22};
//+
Transfinite Surface {25};
//+
Transfinite Surface {23};
//+
Transfinite Surface {24};
//+
Recombine Surface {1, 2, 9, 4, 5, 3, 6, 10, 11, 7, 8, 12, 19, 18, 20, 14, 13, 15, 17, 16,
21, 26, 22, 25, 23, 24};
//+
Extrude {{0, 0, 1}, {0, 0, 0}, Pi/30} {
```

```
 Surface{15}; Surface{16}; Surface{17}; Surface{12}; Surface{13}; Surface{24}; Surface{25}; Surface{21}; Surface{23}; Surface{14}; Surface{26}; Surface{22}; Surface{7}; Surface{8}; Surface{5}; Surface{6}; Surface{4}; Surface{18}; Surface{3}; Surface{20}; Surface{11}; Surface{19}; Surface{9}; Surface{1}; Surface{2}; Surface{10}; Layers{2}; Recombine;
}
//+
Extrude {{0, 0, 1}, {0, 0, 0}, -Pi/30} {
 Surface{15}; Surface{16}; Surface{17}; Surface{12}; Surface{13}; Surface{24}; Surface{25}; Surface{21}; Surface{23}; Surface{14}; Surface{26}; Surface{22}; Surface{7}; Surface{8}; Surface{5}; Surface{6}; Surface{4}; Surface{18}; Surface{3}; Surface{20}; Surface{11}; Surface{19}; Surface{9}; Surface{1}; Surface{2}; Surface{10}; Layers{2}; Recombine;
}

//+
Physical Volume("domain") = {50, 24, 51, 25, 43, 17, 41, 45, 15, 19, 42, 16, 39, 13, 40, 14, 49, 30, 4, 52, 31, 5, 47, 23, 26, 21, 36, 10, 27, 1, 28, 2, 29, 3, 46, 20, 48, 44, 22, 18, 34, 8, 38, 33, 35, 37, 12, 7, 32, 11, 9, 6};
//+
Physical Surface("inlet") = {147};
//+
Physical Surface("outlet") = {201, 110, 115, 206};
//+
Physical Surface("wall_inlet") = {56};
//+
Physical Surface("wall_outlet") = {203, 182, 112, 91, 175, 84, 168, 77, 133, 42, 121, 30};
//+
Physical Surface("wall_top") = {29, 120, 34, 125, 38, 129, 59, 150, 70, 161, 49, 140};
//+
Physical Surface("walls_outlet") = {205, 114};
//+
Physical Surface("walls_tank_bottom") = {107, 198, 184, 93};
//+
Physical Surface("walls_tank_side") = {164, 73, 153, 62, 48, 139};
//+
Physical Surface("front") = {204, 207, 190, 179, 183, 176, 200, 208, 169, 172, 195, 134, 137, 158, 122, 126, 130, 187, 197, 193, 151, 162, 165, 155, 142};
//+
Physical Surface("back") = {113, 116, 99, 92, 85, 88, 81, 78, 109, 117, 104, 67, 46, 43, 39, 35, 31, 96, 106, 102, 74, 71, 60, 64, 51};
```

Appendix B

OpenFOAM boundary conditions for case P5.1

```
/*--------------------------------*- C++ -*----------------------------------*\
  =========                 |
  \\      /  F ield         | OpenFOAM: The Open Source CFD Toolbox
   \\    /   O peration     | Website:  https://openfoam.org
    \\  /    A nd           | Version:  7
     \\/     M anipulation  |
\*---------------------------------------------------------------------------*/
FoamFile
{
    version     2.0;
    format      ascii;
    class       volVectorField;
    object      U;
}
// * * * * * * * * * * * * * * * * * * * * * * * * * * * * * * * * * * * * * //

dimensions      [0 1 -1 0 0 0 0];

internalField   uniform (0 0 0);

boundaryField
{
    inlet
    {
        type                    flowRateInletVelocity;
        volumetricFlowRate        table
        2
        (
        (0 0)
        (500 0.2234)//0.1117//0.0745
        )
        ;

        extrapolateProfile      yes;
        value                   $internalField;
        //type            fixedValue;
        //value           uniform (0 2.5 0);
    }

    outlet
    {
        type inletOutlet;
        inletValue uniform (0 0 0); // this should prevent inflow
        value uniform (0 0 0); // just use for initialization
    }

    "walls_.*"
    {
        type            noSlip;//fixedValue;
        //value           uniform (0 0 0);
    }

    "wall_.*"
    {
        type            slip;
    }
    front
    {
        type            cyclicAMI;
    }

    back
    {
        type            cyclicAMI;
    }
    //#includeEtc "caseDicts/setConstraintTypes"
}

// ************************************************************************* //
```

```
/*--------------------------------*- C++ -*----------------------------------*\
  =========                 |
  \\      /  F ield         | OpenFOAM: The Open Source CFD Toolbox
   \\    /   O peration     | Website:  https://openfoam.org
    \\  /    A nd           | Version:  7
     \\/     M anipulation  |
\*---------------------------------------------------------------------------*/
FoamFile
{
    version     2.0;
    format      ascii;
    class       volScalarField;
    object      p;
}
// * * * * * * * * * * * * * * * * * * * * * * * * * * * * * * * * * * * * * //

dimensions      [0 2 -2 0 0 0 0];

internalField   uniform 0;

boundaryField
{
    inlet
    {
        type            zeroGradient;
    }

    outlet
    {
        type            fixedValue;
        value           uniform 0;
    }

    "walls_.*"
    {
        type            zeroGradient;
    }

    "wall_.*"
    {
        type            slip;
    }
    front
    {
        type            cyclicAMI;
    }

    back
    {
        type            cyclicAMI;
    }
    //#includeEtc "caseDicts/setConstraintTypes"
}

// ************************************************************************* //
```

```
/*--------------------------------*- C++ -*----------------------------------*\
  =========                 |
  \\      /  F ield         | OpenFOAM: The Open Source CFD Toolbox
   \\    /   O peration     | Website:  https://openfoam.org
    \\  /    A nd           | Version:  7
     \\/     M anipulation  |
\*---------------------------------------------------------------------------*/
FoamFile
{
    version     2.0;
    format      ascii;
    class       volScalarField;
    object      epsilon;
}
// * * * * * * * * * * * * * * * * * * * * * * * * * * * * * * * * * * * * * //

//epsilonInlet  0.03; // Cmu^0.75 * k^1.5 / L ; L =0.07*hydraulic diameter

dimensions      [0 2 -3 0 0 0 0];

internalField   uniform 0.000026;//0.000001;//0.000001;

boundaryField
{
    inlet
    {
        type            fixedValue;
        value           uniform 0.000105;//0.000013;//0.000004;//
    }

    outlet
    {
        type            zeroGradient;//inletOutlet;
        //inletValue      $internalField;
        //value           $internalField;
    }

    "walls_.*"
    {
        type            epsilonWallFunction;//epsilonWallFunction;
        value           uniform 1e-12;
    }

    "wall_.*"
    {
        type            slip;
    }
    front
    {
        type            cyclicAMI;
    }

    back
    {
        type            cyclicAMI;
    }
}

// ************************************************************************* //
```

```
/*--------------------------------*- C++ -*----------------------------------*\
  =========                 |
  \\      /  F ield         | OpenFOAM: The Open Source CFD Toolbox
   \\    /   O peration     | Website:  https://openfoam.org
    \\  /    A nd           | Version:  7
     \\/     M anipulation  |
\*---------------------------------------------------------------------------*/
FoamFile
{
    version     2.0;
    format      ascii;
    class       volScalarField;
    object      k;
}
// * * * * * * * * * * * * * * * * * * * * * * * * * * * * * * * * * * * * * //

//kInlet          1.5;    // approx k = 1.5*(I*U)^2 ; I = 0.05 (5%)

dimensions      [0 2 -2 0 0 0 0];

internalField   uniform 0.000957;//0.000239;//0.000106;

boundaryField
{
    inlet
    {
        type            fixedValue;
        value           uniform 0.000957;//0.000239;//0.000106;
    }

    outlet
    {
        type            zeroGradient;//inletOutlet;
        //inletValue      $internalField;
        //value           $internalField;
    }

    "walls_.*"
    {
        //type            kLowReWallFunction;// test1 y 1
        type            kqRWallFunction;//test 3
        value           uniform 1e-12;
    }

    "wall_.*"
    {
        type            slip;
    }
    front
    {
        type            cyclicAMI;
    }

    back
    {
        type            cyclicAMI;
    }
    //#includeEtc "caseDicts/setConstraintTypes"
}

// ************************************************************************* //
```

```
/*--------------------------------*- C++ -*----------------------------------*\
  =========                 |
  \\      /  F ield         | OpenFOAM: The Open Source CFD Toolbox
   \\    /   O peration     | Website:  https://openfoam.org
    \\  /    A nd           | Version:  7
     \\/     M anipulation  |
\*---------------------------------------------------------------------------*/
FoamFile
{
    version     2.0;
    format      ascii;
    class       volScalarField;
    object      nut;
}
// * * * * * * * * * * * * * * * * * * * * * * * * * * * * * * * * * * * * * //

dimensions      [0 2 -1 0 0 0 0];

internalField   uniform 0;

boundaryField
{
    inlet
    {
        type            calculated;
        value           uniform 0;
    }

    outlet
    {
        type            calculated;
        value           uniform 0;
    }

    "walls_.*"
    {
//        type            calculated;
//        value           uniform 0;

      //type            zeroGradient;

      //type          nutLowReWallFunction;// test1 y 2
      type            nutkWallFunction;//test3
      value           uniform 0;
    }

    "wall_.*"
    {
        type            zeroGradient;//test 1-5
        //type  fixedValue;// test 6
        //value uniform 0;
    }
    front
    {
        type            cyclicAMI;
    }

    back
    {
        type            cyclicAMI;
    }
    //#includeEtc "caseDicts/setConstraintTypes"
}

// ************************************************************************* //
```

Appendix C

fvSchemes and fvSolutions

```
/*--------------------------------*- C++ -*----------------------------------*\
  =========                 |
  \\      /  F ield         | OpenFOAM: The Open Source CFD Toolbox
   \\    /   O peration     | Website:  https://openfoam.org
    \\  /    A nd           | Version:  7
     \\/     M anipulation  |
\*---------------------------------------------------------------------------*/
FoamFile
{
    version     2.0;
    format      ascii;
    class       dictionary;
    object      fvSchemes;
}
// * * * * * * * * * * * * * * * * * * * * * * * * * * * * * * * * * * * * * //

ddtSchemes
{
    default         steadyState;
}

gradSchemes
{
//test1, 4 y 5
        limited cellLimited Gauss linear 1;
        default Gauss linear;
        grad(U) Gauss linear;
        grad(p) Gauss linear;

//test2 y 3
    /*default         Gauss linear;
    limited         cellLimited Gauss linear 1;
    grad(U)         $limited; //Gauss pointLinear
    grad(k)         $limited;
    grad(omega)     $limited;*/
}

divSchemes
{
        default none;
        //div(phi,U) bounded Gauss linearUpwindV limited;//tests 1-4;
        div(phi,U) bounded Gauss linearUpwindV unlimited;//test5;
        turbulence      bounded Gauss limitedLinear 1; //test1, 4
        //turbulence    bounded Gauss linearUpwind limited; //test2 y 3
        div((nuEff*dev(T(grad(U))))) Gauss linear;
        div(phi,kt) $turbulence;
        div(phi,kl) $turbulence;

        div(phi,epsilon) $turbulence;
        div(phi,k) $turbulence;
        div(phi,omega) $turbulence;

        div(phi,R)      $turbulence;
        div(R)      Gauss linear;
        div((nu*dev2(T(grad(U))))) Gauss linear;
        div(U,p) Gauss linear;
        div((nuEff*dev2(T(grad(U)))))  Gauss linear;
}

laplacianSchemes
{
        default Gauss linear corrected;
}

interpolationSchemes
{
        default linear;
        div(U,p) upwind phi;
}

snGradSchemes
{
    default         corrected;
}


wallDist
{
    method meshWave;
}

// ************************************************************************* //
```

```
/*--------------------------------*- C++ -*----------------------------------*\
  =========                 |
  \\      /  F ield         | OpenFOAM: The Open Source CFD Toolbox
   \\    /   O peration     | Website:  https://openfoam.org
    \\  /    A nd           | Version:  7
     \\/     M anipulation  |
\*---------------------------------------------------------------------------*/
FoamFile
{
    version     2.0;
    format      ascii;
    class       dictionary;
    object      fvSolution;
}
// * * * * * * * * * * * * * * * * * * * * * * * * * * * * * * * * * * * * //

solvers
{
    p
    {
        solver          GAMG;
        smoother        GaussSeidel;
        tolerance       1e-6;
        relTol          0.1;
    }

    "(U|k|kl|kt|omega|epsilon|v2|f|R).*"
    {
        solver          smoothSolver;
        smoother        symGaussSeidel;
        tolerance       1e-7;
        relTol          0.1;
    }
}

SIMPLE
{
    nNonOrthogonalCorrectors 0;
    consistent      yes;

    residualControl
    {
        U                   1e-5;
        p                   1e-6;
        "(k|kl|kt|epsilon|omega|v2|f|R)" 1e-6;
    }
}

relaxationFactors
{
    fields
    {
        p                   0.3;
    }
    equations
    {
        U                   0.7;//
        "(k|kl|kt|omega|epsilon|v2|f|R)" 0.7;
    }
}

// ************************************************************************* //
```